**Improving contrast in biological imaging: time-resolved microscopy and protein-targeted dendrimers.**

BY
NIVRITI GAHLAUT
B.Sc. St Stephens College, University of Delhi, New Delhi, India, 2004
M.Sc. Indian Institute of Technology Delhi, New Delhi, India, 2006

THESIS
Submitted as a partial fulfillment of the requirements
for the degree of Doctor of Philosophy in Chemistry
in the Graduate College of the
University of Illinois at Chicago, 2012
Chicago, Illinois

Defense Committee:
Lawrence Miller, Chair and Advisor
Leslie Wo-Mei Fung
Wonwho Cho
Preston Snee
Seungpyo Hong, Biopharmaceutical Sciences

This thesis is dedicated to
my mom and dad for their unconditional love and support.

## AKNOWLEDGEMENTS

There are many people I would like to thank for making this doctorate possible. First of all my advisor, Prof. Larry Miller who has been a great mentor to me. His patience, support and guidance during all these years has made this thesis happen. I would like to thank my committee members Dr. Leslie Fung, Dr. Wonhwa Cho, Dr. Preston Snee for their valuable inputs. A special thanks to Dr. Seungpyo Hong for his support. Also, thanks to the Department of Chemistry staff and specially professors that contributed to my growth.

I'm indebted to my labmates, Harsha Rajapakse, Laura E. Pedro-Rosa and Megha Rajendran who were there for me all these years, during the good times and the bad ones. Grad school would have been much harder without their love, friendship, and their valuable advice regarding research and my personal life. Also, a special thanks to the rest of the people in the Miller Group.

Thanks to my friends Mridusmita Saikia and Amrita Banerjee for all the fun times in Chicago and to Nishtha Srivastava for lending me a shoulder to cry on when I needed one. I would like to thank my dad, my sister Romika Gahlaut and my fiancé Barun Chakrabarty for their unconditional love and support. Last but definitely not the least, thank you ma for all your love and always having faith in me and for making me what I am today.

## TABLE OF CONTENTS

**CHAPTER** **PAGE**

**CHAPTER** **PAGE**

## LIST OF TABLES

**TABLES** **PAGE**

## LIST OF FIGURES

**FIGURE** **PAGE**

**FIGURE** **PAGE**

## LIST OF ABBREVIATIONS

| | |
|---|---|
| CCD | Charge-coupled device |
| $CH_3CN$ | Acetonitrile |
| cs124 | Carbostyril 124 |
| DCM | Dichloromethane |
| DMF | Dimethylformamide |
| DMSO | Dimethylsulfoxide |
| DTT | dithiothreitol |
| EDCI | 1-ethyl-3-(3-dimethylaminopropyl) carbodiimide hydrochloride |
| EDTA | Ethylenediaminetetraacetic acid |
| eDHFR | *E. coli* DHFR |
| FRET | Föster resonance energy transfer |
| FBS | Fetal bovine serum |
| GFP | Green fluorescent protein |
| HBTU | O-Benzotriazole-N,N,N',N'-tetramethyl-uronium-hexafluoro-phosphate |
| HOBt | N-Hydroxybenzotriazole |
| HPLC | High performance liquid chromatography |
| ICCD | Intensified charge-coupled device |
| LBT | Lanthanide binding tag |
| LC | Lanthanide complex |
| LED | Light emitting diode |

| | |
|---|---|
| LRET | Luminescent resonance energy transfer |
| NA | Numerical aperture |
| NADPH | Nicotinamide adenine dinucleotide phosphate |
| NaOH | Sodium hydroxide |
| NaOMe | Sodium methoxide |
| PAMAM | Poly amidoamine |
| PPI | Poly propyleneimine |
| ROI | Region of interest |
| SNR | Signal to noise ratio |
| TEA | Triethylamine |
| TMP | Trimethoprim |
| TRL | Time-gated luminescence |
| TTHA | Triethylenetetraminehexaacetic acid |
| UV | Ultra violet |

**Summary**

This dissertation describes the development of two very different strategies for improving the quality of biological imaging. The first is the development, optimization and characterization of a time-resolved luminescence microscope. Time-resolved luminescence (TRL) microscopy can image signals from lanthanide coordination complexes or other probes with long emission lifetimes, thereby eliminating short-lifetime (<100 ns) autofluorescence background from biological specimens. However, lanthanide complexes emit far fewer photons per unit time than conventional fluorescent probes, making it difficult to rapidly acquire high quality images at probe concentrations that are relevant to live cell experiments. This section of my thesis describes the development, optimization, and characterization of a TRL microscope that employs a light-emitting diode (LED, $\lambda_{em}$ = 365 nm) for pulsed epi-illumination and an intensified charge-coupled device (ICCD) camera for gated, widefield detection. Europium chelate-impregnated microspheres were used to evaluate instrument performance in terms of short-lifetime fluorescence background rejection, photon collection efficiency, image contrast, and signal-to-noise ratio (SNR). About 200 nm microspheres were imaged within the time resolution limit of the ICCD (66.7 ms) with complete autofluorescence suppression. About 40 nm microspheres containing ~400 chelate molecules were detected within ~1 s acquisition times. A luminescent terbium complex, Lumi4-Tb®, was introduced into the cytoplasm of cultured cells at an estimated concentration of 300 nM by the method of osmotic lysis of pinocytic vesicles. Time-resolved images of the living, terbium complex-loaded cells were acquired within acquisition times as short as 333 ms, and the effects of increased exposure time and frame summing on image contrast and SNR were evaluated. The performance analyses show that TRL microscopy

is sufficiently sensitive and precise to allow high-resolution, quantitative imaging of lanthanide luminescence in living cells under physiologically relevant experimental conditions.

The second part of my dissertation concerns the synthesis and characterization of monovalent, ligand-functionalized, dendrimer-encapsulated gold particles as potential probes for correlated fluorescence and electron microscopy. PAMAM dendrimer are versatile nanostructures that offer several features which can be leveraged to design useful biological probes. The terminal surface amines can be functionalized with multiple fluorophores or other functional groups. Cystamine core, PAMAM denrimers can be reduced, presenting a single thiol that can be coupled to a targeting ligand monovalently, which is important because multivalent probes having more than one targeting ligand can lead to protein dimerization or oligomerization. To achieve monovalent functionalization, we developed a synthetic protocol where cystamine core PAMAM dendrimers were first labeled multivalently with fluorophores, then subsequently reduced to obtain two dendrons with exactly half the molecular weight of the original dendrimer. The dendrons each possess a single sulfhydryl group that serves as a point of attachment for monovalent linkage to thiol-reactive biotin or TMP. Another property of PAMAM that we sought to exploit for probe development is their ability to encapsulate and stabilize metal and semiconductor nanoparticles. Gold nanoparticles 1 -3 nm in diameter have been shown to be effectively encapsulated inside generation 4 (G4) and higher dendrimers. In this chapter, the synthetic strategies for functionalizing cystamine core G4 and G5 PAMAM dendrimers monovalently with a protein targeting ligand and with multiple fluorophores as well as templating nanoparticle growth are presented.

# Chapter 1

# INTRODUCTION

### 1.1 Contrast in cellular imaging

Modern biology seeks to link cell structure, development, and function to the activity of individual genes, proteins, or other biochemical species (1). Microscopic imaging methods are critical for resolving the structures of molecular complexes in fixed cells or tissues, or for dynamically visualizing the motions and even interactions of biomolecules in living cells. Electron microscopy (EM) can visualize biological structures at the nanometer scale which is the size of proteins. Optical microscopy, especially fluorescence microscopy, can sensitively detect motions of proteins or other species in live cells but on a hundreds of nanometer length scale. The effectiveness of both methods is substantially enhanced by the use of probes or labels that interact with the illumination source (electrons for EM, photons for fluorescence microscopy) and that can be specifically targeted to proteins or other biomolecules of interest.

The useful information contained in a microscope image is fundamentally related to three quantities: magnification, resolution, and contrast. Magnification is simply the size of the image relative to the size of the specimen. Resolution is a measure of the minimum distance between two objects that allows them to be distinguished from one another. It is directly proportional to the wavelength of the illumination source. Because electron wavelengths are ~$10^5$ times shorter than visible light wavelengths, the resolution of EM is considerably higher (angstrom level) than that of fluorescence or other optical microscopies (~300 nm). Both high magnification and, especially, high resolution, are necessary for extracting information from biological specimens, but these quantities are of little use if contrast is insufficient.

Image contrast is defined as the difference between the signal intensity of an object and the background surrounding it divided by the overall background intensity. Contrast is not an

intrinsic property, rather, it depends on the interaction of the illumination source with the specimen. With fluorescence, this interaction is emission of light following absorption; with EM, the interaction is detected as scattering or diffraction of the electron beam. With both types of microscopy, two general strategies can be followed to increase contrast: 1) synthesis of probes that strongly interact with the illumination source; and 2) modification of the instrument to more sensitively detect specimen changes upon illumination (e.g., to more efficiently collect photons in a fluorescence microscope).

This dissertation presents the results of two projects that shared the common goal of improving contrast in cellular imaging; one, probe-based and the other, instrumental. The probe-based approach entails the synthesis and characterization of dendrimer-encapsulated gold nanoparticles that were designed to label specific proteins for correlative luminescence and electron microscopy (CLEM). The instrumental approach is focused on the development and characterization of a time-resolved luminescence microscope. The following sections present an overview of time-resolved microscopy, the potential benefits of probes for CLEM, and the chemistry of polyamidoamine dendrimers that served as the basis for probe development.

## 1.2 Time resolved luminescence microscopy

### 1.2.1 Principle

Fluorescence has a prominent role in biological microscopy because fluorescent images can be made with relatively high spatial resolution (sub-micron), excellent temporal resolution (<100 ms), and high sensitivity. Fluorescence microscopes can be adapted to study the motions of organelles, proteins, or even single molecules in or on living cells, and specialized techniques such as Förster resonance energy transfer (FRET) can even detect intermolecular interactions.

Most fluorescence microscopes generate contrast by spectrally separating red-shifted fluorescence emission from excitation light, and emission can be seen from either endogenous fluorescent species or from external fluorescent probes. However, the sensitivity and precision of fluorescence microscopy is often diminished by autofluorescence. Autofluorescence can come from endogenous species present in the sample (e.g., amino acids, metabolites), from coverslips, or from other sample containers. One method of eliminating autofluorescence, and thereby improving contrast, is to use time-resolved or time-gated detection to differentiate short-lived (~ns) fluorescence from probe luminescence that has a long (>100 ns) emission lifetime (2).

Time-resolved instruments use a finite pulse of light to excite a sample. Then, the detector is electronically switched on, or unshuttered, after a short interval. This is called the gate delay. The gate delay can be set to be sufficiently long for sample autofluorescence to fully decay. The detector then remains on for a finite interval (the gate width) during which time the signal from the long-lived fluorophore is collected (Figure 1). The output from multiple excitation/emission cycles can be integrated to increase detected signal. Time-resolved detection dramatically increases contrast by increasing the signal-to-background ratio. Most commonly, time-resolved detection is used with lanthanide-based immunoassays and high-throughput screening methods where attomole-levels of analytes can be detected in appropriately-configured luminescent plate readers (3). Importantly, the millisecond-timescale lifetimes of lanthanide probes make the adaptation of conventional fluorescence microscopes for time-resolved luminescence (TRL) detection a fairly straightforward endeavor, especially as compared to time-domain fluorescence lifetime imaging microscopes that resolve nanosecond-scale emission events (4).

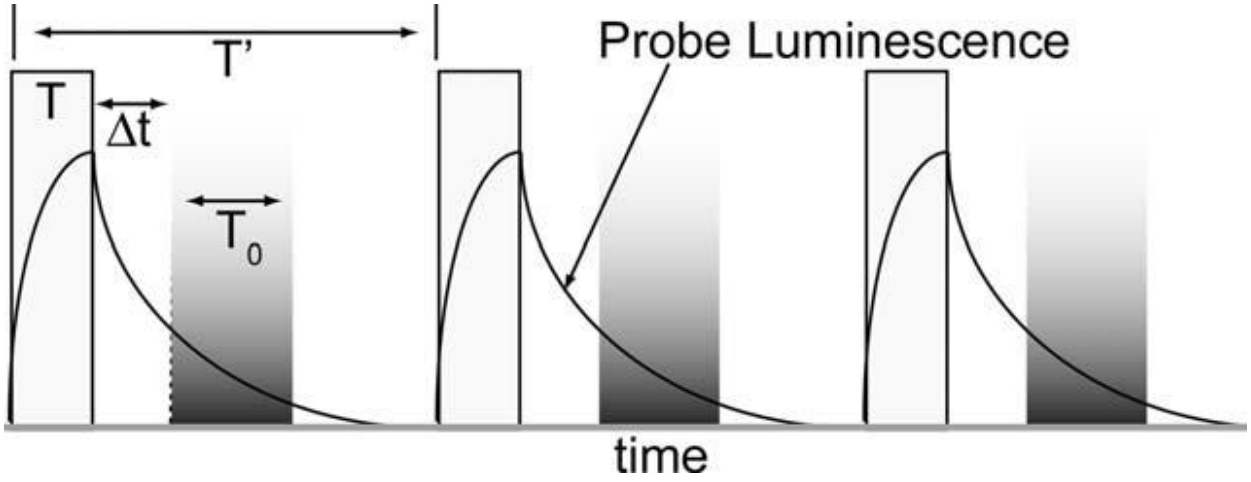


Figure 1: Principle of time-resolved luminescence (TRL) detection. Pulsed light (width = *T*) excites samples. Long-lifetime probe luminescence is detected during an interval ($T_0$) after ashort delay ($\Delta t$) allows decay of scattering and autofluorescence background. Multiple excitation/emission cycles (period = *T*') can be integrated to increase signal.

### 1.2.2 Probes for TRL detection.

The most common emissive probes for TRL application are ligand-sensitized, coordination complexes of lanthanide cations. Lanthanide cations have unique luminescence properties such as long lifetimes (μs–ms) which facilitate TRL detection as well as large Stokes shifts (>150 nm) and multiple, narrow emission bands that make it easy to spectrally isolate signals (Figure 2). These properties originate from their electronic [Xe] 4fn core configurations (n=0-14 for lanthanides). These configurations generate a variety of electronic levels, the energies of which are well-defined due to the shielding of the 4f orbitals by the filled $5s^2 5p^6$ subshells. They are minimally sensitive to the ions' chemical environment. As a result, inner-shell 4f-4f transitions are nearly atom-like and result in narrow-line absorption and emission spectra. Because these transitions are parity-forbidden, the lifetimes of the excited states are long – up to milliseconds for $Tb^{3+}$ and $Eu^{3+}$. However, the parity-forbidden transitions also mean that lanthanide cations by themselves, cannot be efficiently excited. Lanthanide complexes typically incorporate an organic chromophore that absorbs light and indirectly excites the chelated metal via intramolecular energy transfer. Considerable effort has been devoted to develop luminescent lanthanide complexes that are kinetically and thermodynamically stable, water soluble, and easily conjugated to biomolecules. Some $Tb^{3+}$ and $Eu^{3+}$ complexes have relatively high extinction coefficients (>10,000 $M^{-1}$ $cm^{-1}$) and quantum yields (>0.5) in aqueous solution (5-7).

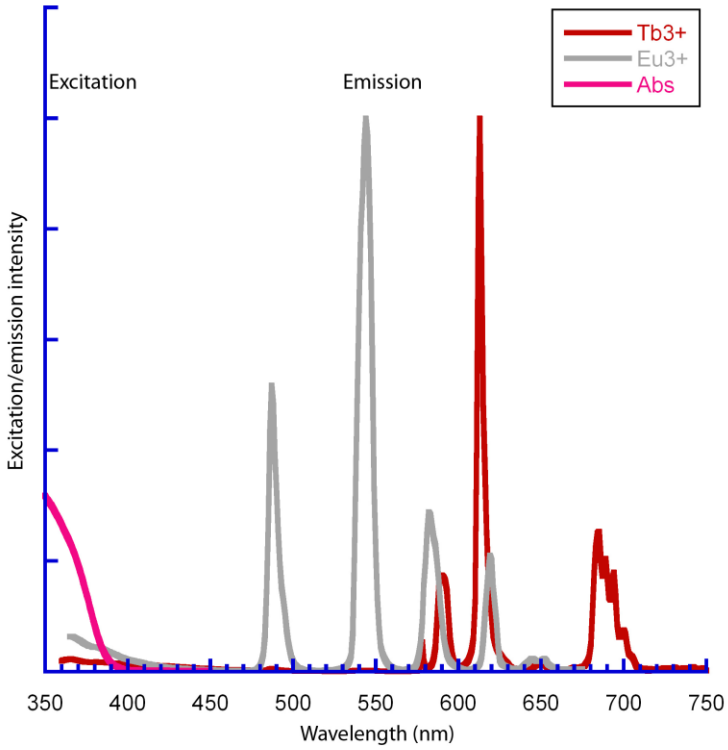


Figure 2: Excitation and emission spectra of some lanthanide complexes. LCs are characterized by large Stokes shift and multiple, narrow emission lines, which make spectral resolution facile. Long emission lifetimes (~ms) enable time-resolved detection.

Other long-lived probes have also been developed for TRL applications, including metal-ligand complexes of platinum and palladium that emit with shorter lifetimes than LCs (100 ns to 10 μs). Furthermore they can be excited with visible light. Phosphorescent dyes with high triplet quantum yields, like eosin or erythrosine, can also be used, but their disadvantage is that they often transfer the energy of the triplet excited state to surrounding biomolecules through singlet oxygen, resulting in quenching of the emission signal (4,8-10).

#### 1.2.2.1 Instrumentation for time-gated luminescence microscopy

A number of investigators have developed TRL microscopes due to the continued advancement in luminescent probe development, and also the clear enhancements in sensitivity achievable with TRL detection. This has resulted in continuous advancement in luminescence probe detection. Further improvements in pulsed excitation sources and fast as well as sensitive, gateable detectors, have made TRL microsocopy a viable technology for bio-imaging applications.

The nature of the luminescent probe determines the choice of excitation source. Most lanthanide complexes are excited between the range of 300 to 370 nm. Early TRL microscopes used a xenon flashlamp or a mechanically chopped mercury lamp to deliver pulsed UV excitation. Flashlamps are advantageous because they are relatively inexpensive, and they deliver much more energy in a shorter period of time compared to a chopper-gated, continuous wave source. The disadvantages of flashlamps are that their pulse repetition rate is limited (<1 kHz), and that the energy can vary from pulse to pulse. Another important disadvantage is that flashlamps emit a long-lived plasma glow that requires gate delays of at least 50 μs. Longer gate delays lead to substantial losses of probe signal, and probes like porphyrins, or ruthenium complexes with ~μs lifetimes, cannot be used.

Another potential excitation source is a pulsed UV laser. Because of the high energy from a UV laser, population inversion can be achieved. A chopper interrupted He-Cd gas laser emitting at 325 nm was used in a TGL microscope built by Phimphivong and colleagues in 1995 (11). An argon ion laser chopped with an acousto-optical modulater (AOM) has also been used for detecting Pt-porphyrins; however this laser emits at 514 nm and is thus not suitable for exciting lanthanide complexes (12).

More recently, UV light-emitting diodes (LEDs) that can deliver ~100 mW power at 365 nm have been developed. This wavelength is compatible for use with some lanthanide complexes (13). LEDs can be modulated with sub-microsecond rise/fall times, and they are relatively easy to incorporate into microscopes. (13-14). Piper and colleagues compared signal-to-noise ratios (SNR) seen in a TRL microscope that used either a flashlamp or a UV LED as the excitation source, and a gated, image-intensified charge coupled device (ICCD) as the detector. Images of *Giardia lambilia* cysts labeled with a europium chelate were acquired with both excitation sources and compared. The rapid LED switch-off permitted a gate delay of 6 µs compared to 60 µs when using the flashlamp, leading to a superior SNR in the case of the former (25 - fold versus 11 - fold improvement over steady state fluorescence imaging (14).

**Detectors**: CCD cameras are generally used as detectors on widefield fluorescence microscopes, while photomultipliers are typical on point-scanning systems (e.g., confocal or multi-photon systems). CCDs do not have fast shuttering capabilities; however, they have been used for time-resolved imaging by placing a chopper-wheel or ferro-electric liquid crystal shutter in the emission light-path. (15-17). A CCD is comprised of a matrix of photosensitive pixels. The interaction of a photon with a pixel leads to the generation of an electric charge. This is converted to voltage using a readout amplifier that is finally converted into a numerical value

using a digitizer. Unlike photomultipliers, conventional CCDs cannot amplify the number of photo-generated electrons. One challenge with imaging lanthanide complexes is that their long emission lifetimes yield low rates of photon emission relative to conventional fluorophores. It is therefore necessary to integrate the emission signal over many cycles to obtain a good quality image. Soini and colleagues demonstrated that up to a 60s integration time might be required with a cooled CCD to obtain images of lanthanide emission with adequate SNR (15).

As an alternative to cooled CCDs, an image-intensified CCD (ICCD) can be used. The image intensifier comprises of a photocathode, a microchannel plate (MCP), and a phosphor screen. When a photon strikes the photocathode, a photoelectron is emitted and is accelerated towards the MCP by an electric field. The MCP consists of channels each about 10 μm in diameter. Once the photoelectron has adequate energy, it displaces secondary electrons from the walls of the MCP. Gain is controlled by adjusting the voltage across the MCP; gain values of more than 10,000X can be reached. The disadvantage is that the resolution is typically less than that of a CCD. Another advantage of ICCD's is that voltage across the MCP can be varied to effectively turn the intensifier on or off, effectively allowing fast shuttering with nanosecond resolution (12). The latest ICCDs have good quantum efficiency (~50% in the visible spectrum) and small effective pixel sizes (~10 μm) that preserve optical resolution. Another possible detector is an electron-multiplied CCD (EMCCD) that has an 'on-chip' or internal amplification. Here, electrons from the pixels are amplified in an extended part of the readout register, Connally and co-workers modified an EMCCD for time-resolved lanthanide imaging (4,14,18); however, with this system, only one excitation/emission cycle could be integrated in a single image frame.

One consequence of lanthanide's long emission lifetimes is that wide-field detection is typically required because point scanning would require exceedingly long image acquisition times. Thus, most of the reported TRL microscopes comprised modifications of epi-fluorescence systems, although Saavedra and coworkers developed a time-resolved total internal reflection microscope (11). Here, excitation was done using a mechanically chopped He-Cd laser emitting at 325 nm and the CCD was temporally gated with a liquid crystal shutter. This set-up was used to study emission from mouse 3T3 cells with a $Tb^{3+}$ chelate as the probe (11). Time-resolved, multiphoton scanning microscopy based on shifting the detection pinhole to collect delayed luminescence from a position lagging the rastering laser beam was recently reported by Ramshesh and Lemasters (19). In this case, an unmodified commercial laser scanning confocal/multiphoton microscopy was used. The detection pinhole was slightly displaced compared to the rasting laser beam to collect only delayed luminescence. Luminescence of microspheres containing europium ($Eu^{3+}$) was compared to that of short-lifetime green-fluorescing microspheres (19).

LCs have been imaged within living cells using TRL microscopy with pulsed, near-UV single photon or two photon excitation, and live-cell TRL microscopy in the microsecond domain has been demonstrated using platinum complexes (8). While these early studies showcased the ability to discriminate probe emission from autofluorescence background, the potential disadvantages of reduced signal have not been addressed. The signal to-noise ratio (SNR) is one measure of microscope image quality, and SNR cannot exceed the square root of the number of photons/pixel (39). This is because even when there are no sources of background or detector noise present, there is an intrinsic noise associated with the signal (S), called the shot noise, that follows poisson statistics. This shot noise increases with increase in signal and is

equal to the square root of the signal. When no other noise is present, SNR is given by $S/S^{1/2}$, or $S^{1/2}$. Given the low rates of photon emission seen with lanthanide probes, the SNR achievable with TRL microscopy may be substantially lower than that observed with conventional, steady-state fluorescence microscopy under conditions of probe concentration and image acquisition time that are relevant to live cell imaging. This is a question that had not been previously addressed, and is the subject of Chapter 2 of this dissertation.

### 1.3 Correlated Fluorescence and electron microscopy

The development of new fluorescent probes and fluorescent microscopes has greatly improved our knowledge of cell biology. Brighter and more stable fluorescent probes have been developed for tagging a protein of interest; furthermore there have been improvement in instrumentation for monitoring these probes. These advancements have helped in studying protein colocalization, function, and turnover. However, the spatial resolution of any optical system is limited by diffraction which is given by the Abbe limit,

$$d = \frac{\lambda}{2(n * \sin\theta)}$$

where, $d$ is the diffraction limit, $n$ is the refractive index of the medium and $\theta$ is the half-angle of the optical objective lens. The denominator $n*\sin\theta$ is called the numerical aperture (NA) and can reach about 1.4 in modern optics; hence, the Abbe limit is roughly $d = \lambda/2$ . Thus, imaging green light with a wavelength of 500 nm, $d$ comes to 250 nm, which means that if two objects are less than 250 nm apart, they will not be resolved (20). To overcome this problem, super resolution technique which beat Abbe's diffraction limit have been developed. Methods like 4Pi and STED sharpen the focal spot whereas PALM and STORM use photochemical

switching and localization of single molecules (21). With these methods, nanoscale spatial information is now accessible. This is in contrast to electron microscopy that has traditionally been used to observe biological structures at sub-diffraction limit resolution has been to use electron microscopy (EM)(1, 22-23).

An electron microscope uses the interaction of a beam of electrons with the sample to produce a magnified image. Due to the much smaller ($10^5$-fold) wavelength of an electron compared to a visible light photon, ~pm resolutions are theoretically possible with EM. Practically, however, ~nm resolutions are achieved with EM imaging of biological specimens. Transmission electron microscopy (TEM) uses an electron beam to illuminate an ultra-thin (~100 nm) samples. As the beam passes through the specimen, it is diffracted, and this diffraction pattern can be detected to reveal the fine structural details such as the shape of a multi-protein complex. Whereas TEM detects transmitted electrons, scanning electron microscopy (SEM) produces image by collecting secondary electrons or backscattered electrons that are emitted by a surface following raster scanning with a beam of primary electrons. Contrast in biological EM can be enhanced by staining specimens with heavy metals (such as lead, tungsten, or molybdenum) or by labeling structures with gold nanoparticles that interact strongly with electrons. SEM specimens must be made conductive, usually by sputtering a thin layer of gold over the surface (24,25).

### 1.3.1 Importance

Correlative light and electron microscopy is a multimodal technique which has the potential to combine the benefits of both fluorescence and electron microscopy (Table 1). Fluorescence microscopy can be used for imaging large areas at fast rates, and for imaging multiple probes in live cells. On the other hand, EM can only be used on fixed cells or tissues,

but it can image both labeled and unlabeled structures, which means that in addition to the probe, other structures in the cell can be visualized at high resolution. Combining these two techniques can give information about processes occurring inside the cell and this can be followed up at high resolution at the ultrastructural level to get more insight into the location of protein and other subcellular structures. Because of their additive nature, the two techniques were originally performed on separate specimens to determine correlation out of the collective data. Correlative light and electron microscopy, however, combined different kinds of LM and EM of the same fixed or frozen cell sample (26).

**Table 1: Imaging features of fluorescence and electron microscope**

| | Fluorescence microscopy | Electron microscopy |
|---|---|---|
| **Resolution power** | + | +++ |
| **Observation of living cells** | + | - |
| **Identification of labeled structures** | + | + |
| **Identification of unlabeled structures** | - | + |

Table 1 (26)

Preparing samples for CLEM involves a number of steps. The electrons that are used to excite the sample in the EM can be easily scattered so the instrument has to operate in a vacuum. To protect the sample from structural changes, it has to be fixed and embedded within a resin. The sample then has to be dehydrated as most resins don't mix with water. High pressure freezing is the most favored method for fixing cells. The advantage with very fast cooling is that crystalline ice that can be destructive to the cells is not formed. Dehydration can then be done at

low temperature using a process called freeze substitution where an organic solvent is added. To stain the cells, flourescent dyes can be added in the organic solvent. The cells are then studied by LM and the cell of interest can be identified by using coverslips with spatial coordinates. Immuno-EM labeling is then done followed by embedding within a resin and sectioning. Pre-embedding immunolabeling is done by permeabilizing the cells with weak detergents. Post-embedding immunolabeling is also an option, although detection efficiency is lesser as only antigens at the resin surface will be labeled (27-29).

An interesting development in the field of CLEM is the integration of a fluorescence light microscope in an EM by Gerritson et al.(30). Here, a laser scanning fluorescence microscope was integrated into a TEM, leading to a reduction in the time of experiment and less difficulty in the probing of the specimen.

### 1.3.2 Probes

There are three main categories of contrast enhancement for correlative LM and EM: i) fluorescence photooxidation probes; ii) signal amplification of enzymes; and iii) particle-based probes.

#### 1.3.2.1 Fluorescence photooxidation

Some fluorescent compounds, can generate oxygen radicals when illuminated. These radicals can then be used to oxidize diaminobenzidine (DAB). Oxidized DAB can be made electron dense through treatment with osmium tetraoxide, which shows uniform staining with little granularity and hence is a suitable probe for EM.

There exist small organic dyes that naturally intercalalate with cell structures and can diffuse easily have been used as probes. An example is Lucifer yellow, which can diffuse

through the cell, and thus helps in delineating the cell in fluorescent imaging. Some fluorescent lipid dyes that can intercalate into vesicles have also been used. An example is FM1-43, which targets membranes by becoming fluorescent after partitioning into the hydrobhobic membrane environment. It has been used for monitoring exocytosis, endocytosis, and endosomal traffic.

Eosin is a tetrabromine derivative of fluorescein that is both fluorescent and efficiently generates oxygen radicals. It can be conjugated to various molecules like antibodies or phalloidin for specific targeting. Capani et al. (31) used eosin conjugated to phalloidin to study actin cytoskeleton in dendritic spines at high resolution using EM and LM.

Genetic-based tags, such as GFP, are widely used for fluorescence imaging; however they are not suitable as probes for EM because reactive oxygen generation is very low. Recently, "miniSOG", a small fluorescent flavoprotein which generates singlet oxygen was used by Tsien et al. (32). Another example is using recombinant proteins genetically labeled by inserting a Cys4 sequence and then exposing the cell to ReAsH, which is a biarsenical non-fluorescent derivative of resorfurin which is nonfluorescent. It binds with high affinity and specificity to the Cys4 motif, after which it becomes fluorescent and has shown to photoconvert DAB. Also, because labeling is carried out in live cells, fixation method can be stringent and permeabilization is not required, which preserves the ultrastructure.

**1.3.2.2 Enzymatic-based methods**

Enzyme-based methods used in combination with immunolabeling are a more traditional method of imaging proteins within cells. Two commonly used enzymes for imaging are horse radish peroxidase (HRP) and alkaline phosphatase that can be targeted to proteins by conjugating them to antibodies. HRP catalyzes a reaction that uses DAB and $H_2O_2$ as substrates; and this

leads to the formation of an amorphous polymer that can be stained by osmium tetraoxide and images with electron microscopy.

The disadvantage of photoconversion methods compared to enzyme-based methods is that they are generally not sensitive enough for imaging with electron microscopy. Several fluorescent molecules like fluorescein cannot be used as they are poor singlet oxygen generators. Although eosin is a potent singlet oxygen generator, it doesn't have a high fluorescent quantum yield for effective fluorescence imaging. A major disadvantage with the enzyme based method is that the diffusion of the reaction product away from the reaction site decreases the resolution.

**1.3.2.3 Particle based methods:**

Quantum dots (QDs) are inorganic nanocrystals that can emit or absorb light at different wavelengths depending on their size. They are also suitable probes for EM because the cores, consisting of elements such as CdSe, CdTe or Au are electron dense. Also, they can be conjugated to antibodies through the water soluble coating on the surface. Mostly, QDs bound to streptavidin are used to bind to a biotinylated antibody, which in turn is bound to the protein of interest (33).

The traditional particle-based method for protein localization in EM uses antibody-targeted, electron-dense gold colloids. Gold probes 1-3 nm in size, referred to as 'Fluoronanogold', have been made that are covalently linked to a fluorophore and a Fab fragment (34-36). Because of the probe's small size, immunolabeling is more efficient. Colloidal gold-antibody conjugates have been used for EM imaging of microtubules in leukocytes (37). One disadvantage of current particle-based methods is that antibody-mediated targeting yields a

relatively small density of labels on protein structures, and this limits both contrast and resolution (38).

In Chapter 3 of this dissertation, the possibility of using ligand-functionalized, polyamidoamine (PAMAM) dendrimers as protein-targeted probes is explored. Such probes would yield high targeting specificity, and because they are much smaller than antibodies, would allow for high density labeling. Furthermore, PAMAM dendrimers can be functionalized with fluorophores or serve as templates for gold nanoparticle formation, possibly enabling a novel strategy for CLEM. The following sections discuss the chemistry and biological applications of PAMAM dendrimers.

**1.4 Dendrimers**

Synthetic polymers are traditionally classified as linear, cross-linked or branched. Although considerable progress has been made in polymer synthesis, in general these types of materials are polydisperse i.e. they have a wide range of molecular weights. In the past 30 years, a type of macromolecular structure called dendritic macromolecules have been developed (39). They are unique in that they are monodisperse and have well-defined molecular structures (39) .

Dendrimers are monodisperse, highly symmetric macromolecules with 3-D structure containing exponential numbers of dendritic branches coming out of a central core. In fact, the name comes from the Greek word *Dendron* meaning ‘tree’ and *meros* meaning part. A dendrimer has three main structural features: (a) an initiator core (b) an interior layer composed of repeating units or branches radiating out of the initiator core, and (c) terminal groups at the surface consisting of a high number of potentially reactive sites (Figure 3). Each branch signifies a generation of the dendrimer (40, 41) .

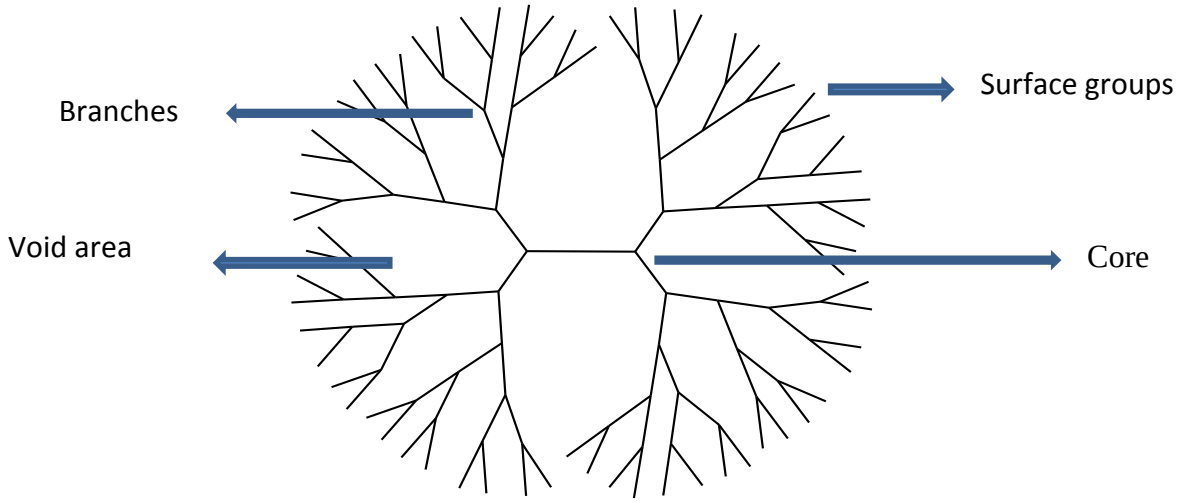


Figure 3: schematic representation of a generation 4 dendrimer.

Mostly dendrimers are synthesized by the repetition of a two-step reaction sequence. One is the generation growth step and the other is the activation step. Two main synthetic approaches have evolved over the years. The first one is the divergent synthesis introduced by Tomalia (42). In this case, there is a core site that acts as the origin of the dendron. Currently, this is the preferred route for commercial synthesis. The second route is the convergent synthesis introduced by Frechet and colleagues (43), where from the surface of the denrimer is synthesized and grows inwards towards a single focal point. Multiple dendrons are then reacted with a multifunctional core to get a dendrimer as the product. More than a hundred dendrimer families have been synthesized using these methods (39).

### 1.4.1 Some types of dendrimers:

Depending on their application, dendrimers with different chemical structures can be synthesized to achieve desired properties like solubility or biodegradability. Some examples that

have been used in biological applications include dendimers based on poly(glutamicacid) Pd-porphyrin dendrimers, polpropyleneimine (PPI), polyester, and PAMAM or poly(amidoamine)(44-45). Of all the families of dendrimers that have been synthesized, Tomalia's PAMAM dendrimer family is the first to have been commercialized and has been the most extensively studied and well characterized**.**

PAMAM dendrimers consist of an ethylenediamine core. This core is reacted with methyl acrylate through a Michael addition. Amidation of the resulting esters with ethylenediamine gives a generation 0 dendrimer; successive reactions give higher generation dendrimers (42). The diameter of PAMAM dendrimer increases linearly at a rate of approximately 1 nm per generation. The surface groups, on the other hand, increase exponentially at each generation. Because of this, after some generation size; congestion can occur at the surface leading to closed structures. The highly congested branching in the interiors can effect the conformations of these dendrimers. Lower generation ones are generally disc-like structures while higher generations (> G4) have a more globular shape. It is typically not possible to prepare generations higher than G10 as the exponentially increasing mass of the dendrimer cannot fit into the linearly increasing diameter (46).

PAMAM dendrimers are characterized by a number of unique properties. They are monodisperse, and they have nanoscale sizes and shapes and a high level of structural control that is similar to biological building blocks. For example generation 3, 4 and 5 are very similar in shape and size to insulin, cytochrome C and hemoglobin respectively. Generation 5 and 6 have diameters similar to the lipid bilayer membranes of biological cells. DNA-PAMAM dendrimers form very stable complexes at generations 7-10. Because they are very similar to proteins in terms of size, shape, and functionality; they are sometimes also called artificial proteins. Another

property is the defined number of surface functional groups (Z) which can be used for bioconjugation of drugs, signaling groups, and targeting moieties, either separately or together in ratios that can be modified and optimized. These groups increase as a function of generation level according to the equation $Z=N_cN_b^G$, where $N_c$ is the core multiplicity which is 4 for PAMAM, $N_b$ is branch cell multiplicity which is 2 for PAMAM, and G is the generation (39)

A third very important characteristic is the well-defined empty space in the interior of these sturctures which is suitable for encapsulation of small molecule drugs or metals. Fourth, lower generation PAMAM (G = 1-5) and higher generation PAMAM with neutral or anionic terminal groups are biocompatible. Also, when surface modified with PEGylated surface groups they show low immunogenicity properties. Because of these properties, PAMAM dendrimers have been developed extensively for biological applications, especially in the fields of drug delivery and imaging (47).

### 1.4.2 Applications

**Drug Delivery:** PAMAM dendrimers are well suited for drug delivery because they have narrow polydispersity; because of their nanometer size, they can travel through biological barriers. They can also be used as carriers for drug molecules by either encapsulation or binding them at the surface. Because of their multivalency, relatively large amounts of drugs can be transported. In contrast with other agents for drug delivery like micelles, liposomes, and emulsion droplets, drug molecules can be attached to dendrimers in a well-defined and controlled way (46, 48).

**Imaging:** Gadolinium chelates are paramagnetic which increase the magnetic relaxation rates of surrounding protons. Because of this property, they are commonly used as intravenous

contrast agents for magnetic resonance imaging (MRI). The disadvantage with them is that they are rapidly cleared from the bloodstream, hence their application in time-dependent imaging studies is limited. Also, high doses are needed due to their relatively low molar relaxivity properties, leading to increased toxicity. To overcome some of these limitations, macromolecular agents have been developed. PAMAM are optimal scaffolds for carrying multiple copies of these chelates. One great advantage of these is their increased relaxivity owing to their slower tumbling rate in solution. This high relaxivity can minimize the injected dose of gadolinium ions. Also, the biocompatibility of the dendrimers can be improved by PEGylating the surface. Lauterbur and colleagues (49) were the first to show an *in vivo* application of dendrimer-based MRI contrast agents in the early 1990s. Since then this has become a topic of intense research (50,51).

### 1.4.3 Nanoparticle templating using PAMAM:

Metal nanoparticles or nanoclusters have traditionally been prepared by reduction of metal salts with a reducing agent like sodium borohydride, hydrazine, or $H_2$. However, this route can yield side reactions or agglomeration of particles that result in poor dispersity. One way to achieve more monodisperse metal nanoparticle preparations is to incorporate stabilizing agents like micelles, polymers and organic ligands into the synthesis (52). Ideally, stabilizing agents for metal particle synthesis should have a number of charactheristics. First, they should be chemically inert towards the nanoparticle. Secondly, they should have a well defined size and shape which helps in the controlled growth of the nanoparticle. Third, they should be comprised of elements which will not hinder the characterization of the nanoparticle. Fourth, their surface should be modifiable so that its solubility and selectivity can be tuned. PAMAM dendrimers have all these required characteristics. They were first used in 1998 by Crooks et al. for the

templated synthesis of Cu nanoclusters (53). Since then, much work has been published related to the synthesis, characterization, and applications of dendrimer encapsulated nanoparticles (9, 52).

Nanoparticles prepared by dendrimer encapsulation are remarkable because they have the chemical and physical properties of the nanoparticle as well as the tunable reactivity and solubility of the dendrimer. Also, the mechanism by which dendrimers stabilize nanoparticles is very different from traditional stabilizers because the dendrimers don't passivate or coordinate to the nanoparticle. In the case of dendrimers, nanoparticles are sterically restricted to the dendrimer interior (54). Another advantage is that properties like size and composition of the nanoparticle can be controlled depending on the dendrimer being used and the method of addition of the metals into the dendrimer. In this way, dendrimers can be used for synthesizing monometallic, bimetallic, and semiconductor nanoparticles with dimensions less than 3 nm. Metal nanoparticles of this size have unique optical, magnetic, electrical, and catalytic properties (55).

**Synthesis:** The first step in the synthesis of DENs is complexing the metal ions with the tertiary amines in the interior of the dendrimer. Next, an excess of reducing agent, usually sodium borohydride, is added to reduce the metal to a zero valence state that initiates nanoparticle growth. Functionalizing the dendrimer with non complexing moieties like hydroxyl groups or adjusting the pH to protonate only the acid or amine groups on the surface helps assure that the metal is in the interior (55). Other than chemical reduction, there are several other routes for preparing DENs. It has been shown that UV irradiation can be used for preparing Au and Ag DENs (56,57). One type of DEN can also be converted to another type through an intradendrimer redox displacement reaction. In this case, DENs prepared from one metal like Cu

can be exchanged with another metal like Ag which should be more noble than the first (58). The synthesis of semiconductor DENs has also been demonstrated. For example Crooks, et al. reported the synthesis of CdS DENs where the dendrimer was used for first sequestering $Cd^{2+}$ ions and then reacted with $S^{2-}$. The dendrimer prevents agglomeration of the CdS nanoparticles (59). One important feature to note is the difference between intradendrimer encapsulated nanoparticles where the nanoparticles are present inside a single dendrimer, and interdendrimer nanoparticles. In the second case, multiple dendrimers are used to stabilize the surface of a single nanoparticle. Dendrimers having amines or carboxyl groups at the surface can have a tendency to form both the types (55) .

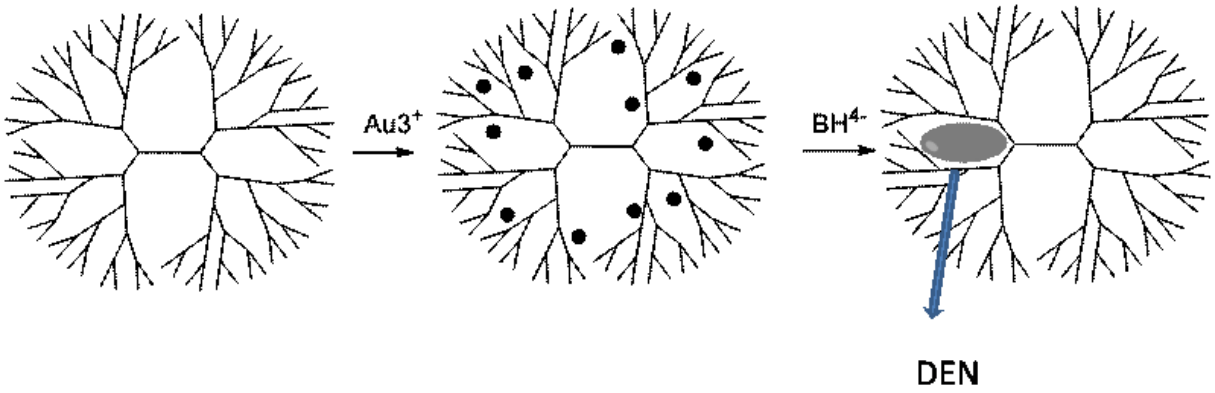


Figure 4: synthesis of a metal nanoparticle.

For **characterization** of DENs, a number of methods are used. Methods like Extended X-Ray Absorption Fine Structure (EXAFS) and X-ray diffraction pair distribution function are sensitive enough to analyze even the smallest DENs. EXAFS is a powerful technique which can give information about the coordination environment of an atom and also information about neighboring atoms. Techniques like EM and even UV-vis can give information about the size of the DENs. The optical plasmon band of DENs in solution can reveal the size of the DENs. For

example, Cu nanoparticles which are less than 3 nm in size do not show a plasmon band in the UV-vis. TEM staining studies and small angle X-ray scattering anaylsis of DENs have also been used to prove encapsulation of 1-3 nm nanoparticles (60).

DENs now have applications in a variety of different fields including catalysis, production of functional coatings, and controlled growth of nanotubes(52, 61). Balogh et al. have reported the synthesis of Au and Ag DENs that are non toxic, fluorescent, water soluble, and stable at biological pH levels. As such, these DENs have a potential as cell biomarkers (62-63). It has also been reported that PAMAM encapsulated Ag complexes are effective antimicrobial agents *in vitro* against some bacteria (64).

# Chapter 2

# TIME RESOLVED LUMINESCENCE MICROSCOPY

## 2.1 Introduction

Time-resolved, or time-gated luminescence (TRL) detection enables bio-assays that are extremely sensitive because of the ability to effectively eliminate autofluorescent background. FRET assays, where long-lifetime terbium or europium species are used as donors and conventional, short-lifetime fluorophores are acceptors, are especially useful for detecting biomolecular interactions. The idea of using TRL detection in microscopic imaging was first introduced in the late 1980's as a means to eliminate the severe autofluorescence that can hinder immunohistological sample imaging (4). Ongoing advancement in lanthanide probe chemistry, and development of more sensitive, gateable cameras has led to a number of research groups explore the use of TRL detection with lanthanides for live-cell imaging. While several proof-of-concept studies have demonstrated visualization of long-lived metal complexes in cells, these studies required either high concentrations (10- 100 μM) in cell medium and/or long (seconds) image acquisition times. Practical live-cell microscopy imposes strict constraints on the number of luminescent species present within cells and the total time available for image acquisition.

In this project, we wanted to explore the maximum sensitivity achievable in lanthanide imaging using a custom-built TRL microscope and analyze its performance in the context of live-cell imaging requirements. We modified an epifluorescence microscope for TRL by incorporating three components: 1) a UV light source for pulsed excitation of the sample; 2) an intensified CCD camera for detection and 3) a delay generator for synchronizing these components. We tested two light sources (pulsed Xe flashlamp, 365 nm LED) and several different objectives in order to optimize TRL image quality, as measured by signal-to-noise ratio (SNR), image contrast, and photon collection efficiency. We assessed the sensitivity and

precision of the instrument as well as the time required to collect high quality images to determine if live cell imaging under conditions of probe concentration and image acquisition time that are relevant to live cell imaging, was possible. We also explored the possibility of diascopic or transmitted fluorescence imaging as a means to detect short-wavelength (~280 nm) excitable terbium binding peptides.

## 2.2 Materials and methods

### 2.2.1 Materials

All chemicals were purchased from Sigma Aldrich (Milwaukee,WI). Lumi4-COOH was a gift from Lumiphore (Richmond, CA). MDCKII epithelial cells were kindly provided by Dr. Jerrold R. Turner, University of Chicago. Dulbecco's modified eagle medium (DMEM), Dulbecco's phosphate buffered saline (PBS), fetal bovine serum, 0.25% trypsin/0.03% EDTA solution, and reagents for pinocytosis/osmoticlysis (InfluxTM reagent, cat. no. I-14402) were purchased from Invitrogen (Carlsbad, CA). NeutrAvidin1-labeled, 40 nm europium beads (cat. no. F20883), NeutrAvidin labeled, 40 nm fluorescein beads (cat. no. F8771), carboxylate modified, 200 nm europium beads (cat. no. F20881), and NeutrAvidin-labeled, 40 nm nonfluorescent beads (cat. no. F8772) were purchased from Invitrogen (Carlsbad, CA). Elemental analysis was performed at Midwest Microlab, LLC (Indianapolis,IN). Biotinylated quartz coverslips were purchased from Microsurfaces (Austin, TX). UV–vis absorption spectra were recorded using a Cary 3000 spectrophotometer (Varian, Palo Alto, CA). Fluorescence emission spectra were recorded using a Fluorolog 3 fluorimeter (Horiba-Jobin Yvon, Edison, NJ). Time-resolved fluorescence measurements to determine luminescent lifetime were recorded using a Victor 3V plate reader from PerkinElmer.

### 2.2.2 Probe Characterization: Eu beads

#### 2.2.2.1 Synthesis of Europium chelate

The europium chelate tris(4,4,4-trifluoro-l-(2-naphthyl)-l,3-butanediono)-bathophenanthroline europium(III), was prepared using published methods (65). Sodium hydroxide (2.0 N, 1.5 ml) was added to a hot solution of 4,4,4 -trifluoro-1-(2-naphthyl)-1,3-butanedione (3 mmol) and europium chloride (1 mmol) in 25 ml ethanol and 2.5 ml $H_2O$ .The hot solution was filtered to remove precipitated sodium chloride, and the solution was combined with a solution of bathophenanthroline (1 mmol) in 10 ml ethanol. The reaction mixture was cooled to room temperature and filtered, and the resulting white precipitate was washed with water and dried under vacuum. The precipitate was recrystallized in acetone/ethanol (1:1). The product was confirmed by CHN analysis (calc. C 61.69, H 3.53, N 2.18; found C 61.95, H 3.39, N 2.21), with a yield of ~ 30%. This was the same Eu-chelate present in the microspheres from Invitrogen.

#### 2.2.2.2 Estimating number of molecules per bead

The absorption spectra of a 2.96 μM solution of the europium chelate in toluene ($\lambda_{max}$= 350 nm, Figure 5) was used to calculate the extinction coefficient of the chelate (44,954 $M^{-1}$ $cm^{-1}$) which in turn was used to estimate the number of europium chelates per bead. The absorbance spectrum of 40 nm diameter europium beads suspended in glycerol ($3.5x10^{12}$ beads/ mL, ~5.8 nM) was measured with the spectrophotometer blanked with a glycerol solution containing an equivalent number of nonfluorescent, 40 nm beads (66). The chelate concentration in the bead solution was calculated to be 2.15 μM from the absorbance at 350nm and the measured extinction coefficient of the chelate. For calculating the average number of molecules per bead, the calculated chelate concentration in the bead solution (2.15 μM) was divided by the bead

concentration (5.8 nM), which yielded an average chelate load of ~370 molecules/bead (2.15 µM/5.8 nM).

#### 2.2.2.3 Lifetime estimation

For estimating the luminescent lifetime, 100 µl aliquots of chelate (~20 nM in toluene) and 40 nm NeutrAvidin-labeled europium beads (~20 nM in water) were pipetted into separate wells of a black 96-well plate. A time-resolved fluorescence plate reader with 340 nm excitation (60 nm bandpass) and 615 nm emission (10 nm bandpass) was used to measure the fluorescence intensity. Intensity values (100 µs integration) were measured at different time delays from 50 µs to 800 µs (50µs increments). Plots of intensity vs. delay time were fit to a single exponential (two parameters) decay with KaleidaGraph v4.0, and the lifetime was estimated from a semi-log fit to the equation: $I(t) = I_0 \exp(-t/\tau)$ with ($R^2 > 0.99$); europium beads, 590 ± 3 µs; tris(4,4,4-trifluoro-l-(2-naphthyl)-l,3-butanediono)-bathophenanthroline europium(III) in toluene, 450 ± 3µs (Figure 5) (2).

#### 2.2.2.4 Quantum yield

The luminescence quantum yield (QY) of tris(4,4,4-trifluoro-l-(2-naphthyl)-l,3-butanediono)- bathophenanthroline europium(III) in toluene (QY =~0.30) was determined by standard methods using quinine sulfate in 1 N sulfuric acid (QY = ~0.546) as a reference chromophore (67). Attempts to determine the QY of europium beads yielded inconsistent results, ranging from 0.04 to 0.15, with a mean value of 0.08 (four measurements).

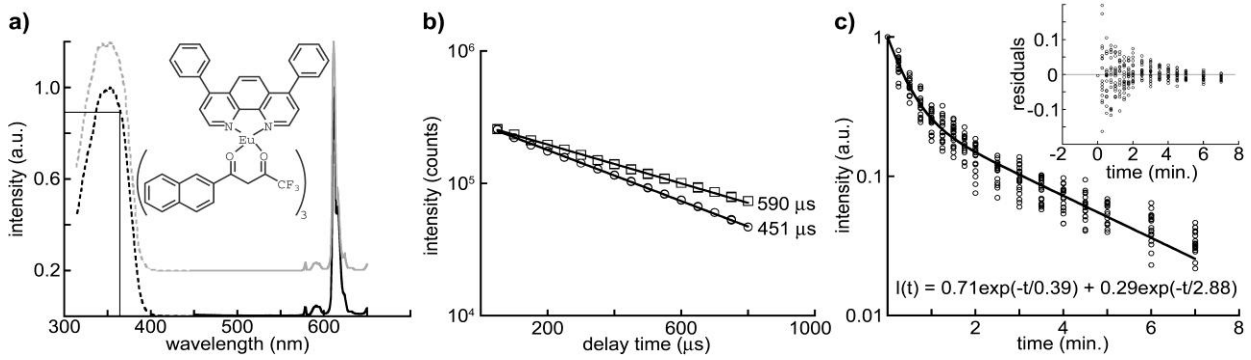


Figure 5: Spectra, luminescent lifetime, and photobleaching kinetics of europium microspheres used in this study. (a) Normalized excitation (dotted) and emission spectra (solid) of 40 nm, NeutrAvidin-labeled europium microspheres (FluospheresTM, cat. no. F20883,Invitrogen) in water (black) and the europium chelate present in the microspheres, tris(4,4,4-trifluoro-l-(2-naphthyl)-l,3-butanediono)-bathophenanthroline europium(III) (structure, inset), dissolved in toluene (gray). The chelate spectra are shown offset for clarity. The absorbance of the beads/chelate is ~90% of maximum at the UV LED emission wavelength (365 nm), as indicated by the lines drawn on the graph. (b) Semi-log plot of intensity vs. delay time for 40-nm europium beads in water (squares) and europium chelate in toluene (circles). The solid lines represent single exponential (two parameter) fits to the data, $I(t) = I_0\exp(-t/\tau)$. The calculated lifetime is shown adjacent to the plotted curves, and three repetitions of the experiment yielded values that agreed within <4%. $R^2$ residuals were greater than 0.99 in all cases. (c) Semi-log plot of luminescence intensity (normalized to initial value at $t = 0$) vs. accumulated irradiation time for 200 nm europium beads. A field of view was exposed to continuous wave LED excitation at the standard illumination intensity (~0.6 W $cm^{-2}$), imaged at successive timepoints, and the net signal intensity determined for 20 single beads at each timepoint. The solid line is a two-exponential (four parameter) fit to the data: $I(t) = a \times \exp(-t/\tau_1) + b \times \exp(-t/\tau_2)$. The bead luminescence decayed with a major component (71% amplitude) of 0.39 min and a minor component (29% amplitude) of 2.88 min. $R^2$ residuals equaled 0.98 and showed no structure (inset). Specific imaging parameters are provided in Table 1.

### 2.2.3 Preparation of Eu bead test specimens

Beads were sonicated for 15 min prior to dilution into $H_2O$ for specimen preparation. An aqueous suspension was prepared that contained 40 nm, NeutrAvidin-labeled europium beads (diluted 1:200 from stock) and 40 nm, NeutrAvidin-labeled fluorescein beads (diluted 1:50 from stock). Ten microliters of the suspension was pipetted onto the surface of a quartz coverslip modified with a polyethylene glycol-biotin surface. After 5 min the coverslip was rinsed with water to remove any beads that were not bound through the Neutravidin- biotin interaction. After drying with $N_2$, the coverslip was sealed to a quartz slide with Valap (1:1:1 Vaseline$^{TM}$:lanolin: paraffin). Carboxylate-modified europium beads (200nm diameter) were diluted 1:5,000 in $H_2O$, and 5 µl was pipetted onto a clean quartz coverslip and allowed to dry in air. A 10 µM solution of AlexaFluor$^{TM}$ 350 ($\lambda_{ex,max}$ = 343 nm, ($\lambda_{em,max}$ = 442 nm) was prepared in water and 20 µl was pipetted onto a quartz microscope slide. The dried coverslip with the bead side facing down was placed onto the slide and sealed with Valap.

### 2.2.4 Preparation of live cell samples

**Cell Culture.** MDCKII cells were cultured in Dulbecco's Modified Eagle Media (DMEM, Invitrogen) supplemented with 10% FBS, 2 mM L-glutamine, 100 U ml$^{-1}$ penicillin and 100 mg mL $^{-1}$ of streptomycin at 37$^{o}$C and 5% $CO_2$. Cells were passaged using 0.25% trypsin/0.03% EDTA solution. To prepare samples for imaging, cells were trypsinized and reseeded at 14,000 cells well$^{-1}$ into eight-well chambered slides and incubated at 37 $^{o}$C and 5% $CO_2$ overnight.

**Probe delivery via osmotic lysis of pinosomes.** A 5 µl aliquot of Lumi4-COOH (800 µM in $H_2O$) was combined with ~1.2 equivalents of $TbCl_3$ (in ~1 µl $H_2O$), vortexed for 5 min, and allowed to stand at room temperature for 30 min. This step affords the chelation of terbium,

rendering the probe luminescent. The metal-labeled Lumi4-Tb solution (~6 µl) was combined with 14 µl of hypertonic growth medium (Influx™ reagent, Invitrogen, prepared according to manufacturer's instruction), yielding a final concentration of Lumi4-Tb equaling 200 µM. MDCKII cells in a single well of an eightwell chambered slide were washed 1X with prewarmed (37°C) PBS and 2X with prewarmed hypertonic solution, respectively. Then, prewarmed hypertonic solution containing Lumi4-Tb was added, and the cells were incubated at 37°C and 5% $CO_2$ for 10 min. The cells were then quickly washed 2X with hypotonic solution (Influx™ reagent, Invitrogen, prepared according to manufacturer's instruction) and allowed to incubate in hypotonic solution for exactly 2 min at room temperature to effect lysis of pinosomes. The cells were then washed 2X with PBS, immersed in DMEM and incubated for ~1 h at 37°C and 5% $CO_2$ before imaging.

**Sample preparation for diascopic illumination**: Glutathione sepharose beads (250 uL beads in IL1β buffer (10 mM HEPES, pH 7.0, 100 mM NaCl, 5 mM beta-mercaptoethanol) + 150 nmol GST-IL1β-S1-$Tb^{3+}$ (glutathione-sepharose beads bound to a fusion protein consisting of glutathione-s-transferase linked to LBT-modified, interleukin 1β, obtained from Prof. Karen Allen lab, Boston University) were vortexed for 2 minutes. 10 µL of the bead suspension was pipetted onto the surface of a quartz coverslip and allowed to dry in air. The dried coverslip with the bead side facing down was placed onto a quartz slide and sealed with Valap

### 2.2.5 Apparatus development and microscope set up

#### 2.2.5.1 Light Source

We compared two light sources: a UV LED and a Xe flashlamp to determine which was the most efficient in illuminating the probe. Power measuring to measure the excitation intensity

in the plane of the sample was done according to a procedure by Singer et al. (68). The measurement was done above the objective turret without an objective present. An adjustable iris with a diameter equal to that of the back aperture of the objective was placed on the turret using an adaptor. A short focal length lens was mounted on top of the iris to collect the light and focus it onto a thermocoupled power meter.

The power density (units in kW $cm^{-2}$) depends upon the transmission curve and field of view of the objective used for imaging. The field of view (FoV) is given by the field number (FN) in mm divided by the magnification of the objective:

$$\text{Fov (mm)} = \frac{\text{FN (mm)}}{\text{Magnification}_{\text{objective}}} \quad (1)$$

Half of the FoV is equal to the radius which can be used to calculate the area of the field of illumination. The detector measures the average power, in pulsed excitation, the peak power is important. The peak power energy was calculated using:

$$E = P_{avg}T \quad (2)$$

where $P_{avg}$ is the average power determined by the detector and T is the reciprocal of the excitation frequency. E is the total energy given in Joules. This is used to calculate the peak power which is given by:

$$P_{peak} = \frac{E}{\Delta t} \quad (3)$$

where $P_{peak}$ is the peak power during the excitation pulse and $\Delta t$ is the duration of the excitation pulse. This can then be used to calculate the power density:

$$\text{Power density} = \frac{P_{peak}}{(\pi r^2)(cm^2)} \quad (4)$$

The power density multiplied by the transmission of the objective (provided by the company) gives the actual power density at the image plane.

**Xenon flashlamp:** A pulsed, Xe flash lamp (Perkin Elmer, model FX 4400) was studied. A 24 V supply powers the lamp controller (Perkin Elmer, PS 4400 power supply and FYD4400 Lite-Pac$^{TM}$) and provides an adjustable reference voltage to modulate the controller output power (400-100 volts). The lamp is externally triggerable (to 1 kHz) and delivers a 1-2 µsec flash with a maximum energy of 1 J at $\lambda_{em}$ = 325- 350 nm. The maximum average power of the lamp is 60W. An adaptor was machined to couple the lamp to a focusing assembly (Newport-Oriel, Inc., model no. 77776). This allowed the light from the lamp to be focused into a 1m x 3mm light guide, and directed into the microscope by a liquid light guide adaptor (Zeiss), providing an even field of illumination.

For power measurement, the lamp was externally triggered at 500 Hz. The average power was 0.5 mW. E was calculated to be 1µJ (T was 0.002s). For calculating $P_{peak}$ the pulse width or $\Delta t$ was taken as 1.5µsec. This gave a value of 0.67 W as the peak power. The FN of the 63X EC Plan NeoFluar objective from Zeiss is 25 mm which gave 0.00124 $cm^2$ as the area of illumination, resulting in a peak power density of 538 W $cm^{-2}$. By taking into account the transmission of the objective (50 %) the power density was estimated to be 269 W $cm^{-2}$.

**UV LED:** A light emitting diode (LED) emitting at 365 nm (UV-LED-365, Prizmatix, Southfield, MI.) provides a collimated output that we measured to equal ~50 mW at the exit window when operated at an injection current of ~400 mA (maximum injection current is 500

mA). The LED circuitry allows for continuous wave emission or external TTL modulation with submicrosecond rise/fall times. The excitation intensity can be adjusted by varying the injection current. We determined the average power density at the sample plane in a manner similar to the flashlamp. The average power was measured to be 1.6 mW at the objective back aperture, yielding an estimated illumination intensity of ~0.6 W $cm^{-2}$ at the image plane.

### 2.2.6 Time resolved luminescence microscope configuration

An epifluorescence microscope (Axiovert 200, Carl Zeiss, Thornwood, NY) was modified with the following components to enable TRL imaging: (69) a light emitting diode (LED) emitting at 365 nm (UV-LED-365, Prizmatix, Southfield, MI); (2) delay generator (DG645, Stanford Research Systems, Sunnyvale, CA); (3) an ICCD, mounted on the side-port of the microscope, and camera controller (Mega-10EX, Stanford Photonics, Palo Alto, CA); and (4) a computer running Piper Control software (v2.4.05, Stanford Photonics). A 100-W mercury arc lamp enables continuous wave fluorescence excitation. Filter cubes containing the appropriate excitation and emission filters and dichroics allowed for wavelength selection. Images were acquired through a 63X objective lens (EC Plan Neofluar, 63X 1.3 N.A., Carl Zeiss).

The camera platform consists of an intensifier with a filmless GaAsP Extreme photocathode (Quantum Efficiency = ~0.4 from 450 to 600 nm, ~.38 at 610 nm) fiber-optically coupled with a 1.6:1 taper ratio to a Sony XX285 CCD sensor. The CCD sensor is a 1,380 X 1,024 array of 6.47 $\mu m^2$ pixels, and the effective pixel size of the intensifier/camera is 10.35 µm. The CCD can be read out at a full-frame rate of 15 frames-per-second with a read noise of 10 electrons rms. The intensifier can be externally gated with a time resolution of 5 ns, and modulation of the multi- channel plate voltage allows for variation in gain levels to a maximum of about 84,000.

The delay generator mediates synchronization of the LED and the image intensifier. Piper Control software (Stanford Photonics, v2.4.05) synchronizes the camera frame clock with an external pulse routed to the delay generator to begin the image acquisition sequence. The delay generator can be programmed to generate a burst of output signals directed to the LED and the intensifier (routed through the camera controller). This configuration allows the user to define the LED pulse width (T) and pulse period (T'), the intensifier gate delay ($\Delta t$), the intensifier gate width ($T_0$), and number of excitation/emission cycles that occur in a single camera frame. The emission signal from multiple cycles is integrated on the CCD and read out to the image capture card of the computer at the end of the frame. The frame length can be varied as multiples of the camera frame clock, from 1 clock (66.7 ms) up to a maximum of 30 clocks (2 s). The camera control software allows for either summation or averaging of an arbitrary number of frames, and generates images in Tagged Image File (TIF) format.

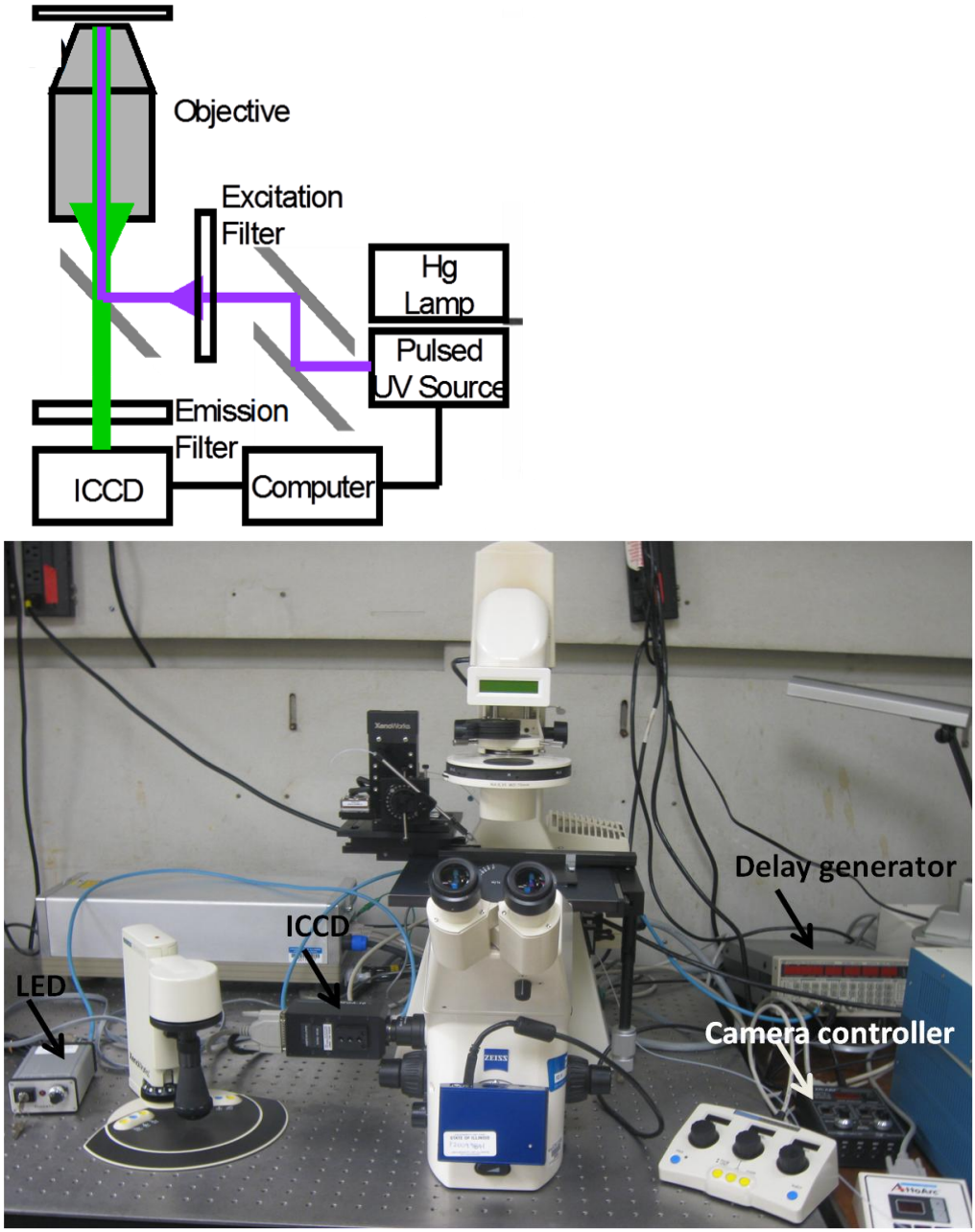


Figure 6: Time-resolved epifluorescence microscope. An epi-fluorescence microscope (Zeiss Axiovert 200M) is equipped with a pulsed excitation source (V-LED-365, Prizmatix, Southfield, MI) and intensified CCD (Stanford Photonics, MEGA-10EX). Intensifier and flashlamp timing are directed by a delay generator (Stanford Research Systems, DG-645) controlled by image acquisition software. Pulse rate (to 1kHz), gate delay, gate width, and CCD frame rate (66.66 msec-2sec) are independently variable.

### 2.2.7 Estimation of background signal from optical components.

To determine if the microscope objectives and/or slides and coverslips used for imaging can generate non-specific, long-lived luminescence background, we measured the mean pixel gray value obtained under equivalent illumination conditions with several objectives and with glass or quartz coverslips. The microscope was configured as described above with the following filter sets: G365 excitation filter, F395 Dichroic, and LP420 emission filter (all filters from Carl Zeiss, Inc.). For testing coverslips and slides, the following settings were used: pulse width, 600 μs; gate delay, 10 μs, burst period, 1300 μs, intensifier gate width, 600 μs. Total integration time was 660 ms (500 excitation/emission cycles) and the intensifier gain voltage was 778 V.

### 2.2.8 Objectives:

An ideal objective is one that has adequate UV transmission (~50% at 350 nm), high NA, >40X (60X or 100X), and very little background. We tested a number of different objectives under the same conditions to see if they were a source of background. No samples were mounted in these studies and the objective being tested was clean, i.e., no oil or other immersion media was used. The same time resolved microscopy configuration mentioned in the set up was used. A G365 excitation filter was used for excitation, also F395 Dichroic and an LP420 emission filters were used. The pulse width was 1500 μs, gate delay was 100 μs, burst period was 3000 μs, and the intensifier gate width was 1390 μs. The integration time was 2s (660 excitation/emission cycles) and the gain level was 778 V.

### 2.2.9 Detector calibration

For each intensifier gain level, the proportionality factor ($g$) relating image intensity values to the apparent number of photons was measured from a graph of variance versus mean intensity for a set of images. To determine variance, a pair of images of a uniform field of a

luminescent sample was collected in rapid succession. A dark frame image was also captured with the LED off. The dark frame was subtracted from each of the paired images to give a new pair of images. One of these was subtracted from the other to give a difference image, leaving mainly Poisson noise with a variance equal to twice the variance of a single image. Similarly, the variance was calculated for different exposure times and plotted against the mean intensity for each image pair giving a slope equal to *g*.

### 2.2.10 Data Collection

For quantitative imaging of 40-nm europium beads, test specimens containing both fluorescein and europium beads were mounted on the microscope and examined through the eyepiece under continuous wave, Hg lamp excitation with a fluorescein filter set ($\lambda_{ex}$ = 480/40 nm, $\lambda_{em}$ = 535/50 nm). Emission from fluorescein beads was visible through the eyepiece, allowing location of the plane of focus. The larger (200 nm) europium beads were visible through the eyepiece under continuous wave excitation ($\lambda_{ex}$ = 365 nm, $\lambda_{em}$ = 620/20 nm), allowing focusing without codeposition of fluorescein beads. TRL images of both 40 and 200 nm europium beads were captured using the 63X EC Plan Neofluar objective and the following filter sets: excitation filter, G365, Carl Zeiss; dichroic, FT395, Carl Zeiss; narrow-pass emission filter, D620/20 nm (Chroma Technology Corp., Bellows Falls, VT). The emission filter effectively transmitted light from 605 to 630 nm with ~80% transmittance at 610 nm (the emission maximum of the europium beads used in this study).

The source and camera timing parameters that were implemented for time-resolved imaging are delineated in Table 2. For all time-resolved images, the illumination intensity at the sample plane was 0.6 $Wcm^{-2}$. For quantitative analysis of emission from 40nm europium beads, multiple images of the same field of view were collected at different exposure times that were

determined by setting the number of frame clocks in the camera control software. Fifty excitation/ detection cycles were implemented per single frame clock of 66.7ms duration. For example, a setting of five frame clocks yielded a total frame length of 333 ms during which time 250 excitation/detection cycles were implemented. Frame summing was implemented with the camera control software to acquire composite images (tagged image file format, .TIF) of one or four frames with pixel depths of 1,024 (10-bit) or 4,096 (12-bit), respectively. The saturation level is 16 bits (pixel depth, 65,536), achieved upon summation of 64 frames. The camera software clamps saturating signals; however, clamping was not evident at the low signal levels observed here. Series of bead images were collected at three different intensifier gain voltages: 778, 889, and 944 V. By correlating these voltages against manufacturer's calibration data, the estimated gain values were 5,000, 21,900, and 45,500, respectively.

| Image or data | Figure 5c | Figure 7 | Figure 8b | Figure 9 | Figure 10a | Figure 10b | Figure 10c | Figure 11b, left | Figure 11b, right | Figure 11c, left | Figure 11c, right |
|---|---|---|---|---|---|---|---|---|---|---|---|
| **$\lambda_{em}$(nm)** | 605-630 | 605-630 | 605-630 | 605-630 | 605-630 | 605-630 | 605-630 | 530-550 | 530-550 | 530-550 | 530-550 |
| **Excitation pulse width (ms)** | 0.600 | 0.600 | 0.600 | 0.600 | 0.600 | 0.600 | 0.600 | 1.500 | 1.500 | 1.500 | 1.500 |
| **Gate delay (ms)** | 0.010 | 0.010 | 0.002 | 0.010 | 0.010 | 0.010 | 0.010 | 0.010 | 0.010 | 0.010 | 0.010 |
| **Intensifier gate width (ms)** | 0.600 | 0.600 | 0.600 | 0.600 | 0.600 | 0.600 | 0.600 | 1.390 | 1.390 | 1.390 | 1.390 |
| **Excitation events** | 50 | 250 | 50 | [a] | 500 | 500 | 500 | 110 | 110 | 440 | 440 |
| **Frame length (ms)** | 66.7 | 333 | 66.7 | [a] | 667 | 667 | 667 | 333 | 333 | 1333 | 1333 |
| **Frames (summed)** | 4 | 4 | 1 | 4 | 4 | 4 | 4 | 1 | 4 | 1 | 4 |
| **Exposure time[b] (ms)** | 30 | 150 | 30 | [a] | 300 | 300 | 300 | 165 | 165 | 660 | 660 |
| **Acquisition time (ms)** | 66.7 | 1333 | 66.7 | [a] | 2667 | 2667 | 2667 | 333 | 1333 | 1333 | 5333 |
| **Intensifier gain (V)** | 778 | 944 | 778 | [a] | 778 | 889 | 944 | 778 | 778 | 778 | 778 |
| **Pixel dimensions** | N/A | 31X31 | 300X300 | N/A | 250X200 | 250X200 | 250X200 | 900X725 | 900X725 | 900X725 | 900X725 |
| **Pixel depth** | N/A | 4096 | 1024 | N/A | 4096 | 4096 | 4096 | 1024 | 4096 | 1024 | 4096 |
| **Contrast (min./max.)** | N/A | 585/1772 | 56/1019[c] | N/A | 160/834[c] | 268/1739[c] | 440/2417[c] | 23/162 | 109/515 | 31/486 | 137/1851 |

Table 2: Summary of detection and image processing parameters for time-resolved images and data presented in the chapter.

[a]The data presented in Fig. 9 were acquired at varying numbers of excitations and gain levels as indicated in the text and figure legend.

[b]Exposure time indicates the total irradiation time of the sample during a single exposure. Frame summing multiplies exposure time accordingly.

[c]Contrast was adjusted to the minimum/maximum pixel gray values using NIH Image J and further enhanced for visual clarity using Adobe Photoshop.

### 2.2.11 Image analysis

Image analysis and processing (cropping, contrast setting) was performed using NIH ImageJ (v.1.34). Further adjustment of contrast, as needed, was performed using Adobe Photoshop (v. 7.0). Image processing parameters (image size, pixel depth, min/max gray values) are provided in Table 2.

For evaluation of 40nm europium beads, images were analyzed visually to locate candidate single beads. As an initial filter, all bright pixel regions that appeared in sequential images were selected for analysis. Bright pixels near the edge of the field of view were excluded to minimize effects of varying illumination intensity. To distinguish between single beads and clusters of multiple beads, we measured the net integrated intensity of a 3 X 3 pixel region of interest (ROI) centered on each candidate bead in a four-frame image collected at high gain level (944 V) with a frame length of 2 s (1,500 exposures per frame, total image acquisition time = 8 s).

To calculate net integrated intensity, local per-pixel background (b) was first determined by measuring the raw intensity in a 25 X 25 pixel ROI centered on a single bright pixel region and subtracting from this the net integrated intensity in a central 3 X 3 box (Figure 7), and b was given by the following equation (61):

$$b = \frac{\sum_{-12}^{12}\sum_{-12}^{12} I_{x,y} - \sum_{-1}^{1}\sum_{-1}^{1} I_{x,y}}{616} \qquad (5)$$

Pixel intensities within the 3 X 3 pixel ROI centered on the bead were summed to give the raw intensity. Net intensity (S) was calculated by subtracting the background in the 3 X 3 box from the raw intensity:

$$S = \sum_{-1}^{1} \sum_{-1}^{1} I_{x,y} - 9b \quad (6)$$

We then generated a histogram of net integrated intensities that revealed three regions corresponding to single beads and clusters of two or three beads. The histogram analysis revealed the location of 29 single beads within the field of view, and the ROIs containing these single beads were retained for subsequent analysis of the remaining images.

A similar histogram analysis was performed on an image of 200nm beads to assure evenness of illumination throughout the field of view. From the histogram analysis, 25 beads were identified that were distributed evenly throughout the image, and the net integrated bead intensity was measured to be 26,600 ± 2,660 (mean±σ.). No particular trend in measured intensity was observed in different regions of the image, indicating uniform excitation intensity across the field of view.

Images of 40 nm beads were further evaluated by calculating the net number of photons collected from each bead. Net integrated signal intensity, S, was divided by the appropriate camera gain factor, g. When appropriate, this value was divided by the number of frames summed because frame summing proportionally scales the pixel depth of the image, and net photons per bead is given by:

$$\mathrm{N} = \frac{\mathrm{S}}{\mathrm{g} * \mathrm{no.frames}} \quad (7)$$

Contrast (C) is defined as the magnitude of S relative to the magnitude of the expected Poisson fluctuations in background over the central 3 X 3 pixels of a bead ROI:

$$C = \frac{S}{\sqrt{9b}} \quad (8)$$

SNR was defined as the mean signal divided by the error in the signal, and mean signal was calculated as the net integrated intensity divided by the area of the central 3 X 3 pixel array. The error in the signal was taken to be the standard deviation in pixel gray value of the local 25 X 25 ROI because this gave a larger sample size than the 3 X 3 array. SNR was then calculated for each 40nm bead in each image as:

$$SNR = \frac{\frac{S}{9}}{\sigma_b} \quad (9)$$

Analogous measurements (net photons, contrast, SNR) were made of images of MDCKII cells loaded with Lumi4-Tb. The net, per-pixel emission signal intensity was calculated according to the equation: $S = (\mu_{signal} - \mu_{bckg})$, where, $\mu_{signal}$ is equal to the mean pixel gray value in a ROI corresponding to the area of a cell, and $\mu_{bckg}$ is equal to the mean pixel gray value in a nearby ROI of equivalent area. The mean number of photons per pixel in a given cell was calculated by dividing the net intensity by the appropriate camera gain factor and number of frames: N = S/(g * no. frames). Contrast was defined as the net signal intensity divided by the square root of the mean pixel gray value in the background region: $C = S/(\mu_{bckg})^{1/2}$. For a given cell in an image, SNR was defined as the mean signal divided by the error in the signal. Because signal levels varied widely over the area of a cell (e.g., between cytoplasm and nucleus), the signal error was taken to be the standard deviation in pixel gray value for a neighboring background ROI, and $SNR = S/\sigma_{bckg}$. The mean values of photons per pixel, contrast and SNR were reported from analysis of six cells in each image (Table 3).

| Image | Photons per pixel | Contrast | SNR |
|---|---|---|---|
| **Fig. 11b, left** | 10.1/0.8 | 8.2/0.7 | 1.9/0.15 |
| **Fig. 11b, right** | 8.4/0.7 | 13.9/1.2 | 2.9/0.22 |
| **Fig. 11c, left** | 44.3/3.8 | 30.0/2.5 | 4.0/0.45 |
| **Fig. 11c, right** | 41.6/3.6 | 58.0/4.9 | 6.2/0.81 |

Table 3: Summary of quantitative analyses of cell images shown in Figure 11. Data are presented as mean ± s.e.m. for each value, calculated as described in Materials and Methods from six cells in each image. Data collection and image processing parameters are given in Table 2.

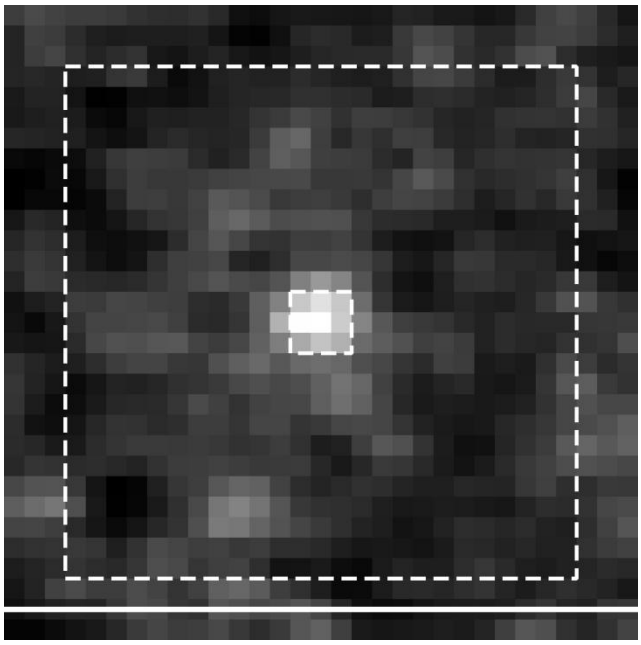

Figure 7: Schematic explaining the measurement regions described in the text. The micrograph shows the time resolved image of a single, 40 nm europium chelate-impregnated polystyrene bead. Dashed lines show the pixel area boundaries. *Raw bead intensity* is the sum of pixel values in the central 3 X 3 box. For measuring the local per pixel background, a 25 X 25 pixel neighborhood excluding the 3 X 3 box was used. Subtracting the background in the 3 X 3 box (i.e. 9b) from the raw bead intensity gave the *Net integrated bead intensity* (S). The TRL imaging parameters for all images and data are given in Table 2. Scale bar, 10 μm.

### 2.2.12 Photobleaching analysis

To determine the photobleaching kinetics of tris(4,4,4-trifluoro- l-(2-naphthyl)-l,3-butanediono)-bathophenanthroline europium(III) in bead specimens, 200nm europium beads were dispersed onto coverslips, mounted on the microscope, and exposed to continuous wave LED illumination at the standard intensity used in this study (0.6 W $cm^{-2}$). A field of view was imaged at successive timepoints, and the net signal intensity (Eq. 6) determined for 20 single beads in each successive image (see Table 2 for imaging parameters). The measured signal intensities were normalized to the initial values (t = 0), plotted against accumulated irradiation time and fit to a two-exponential (four parameters) decay curve with KaleidaGraph v4.0: $I(t) = a * \exp(-t/\tau_1) + b * \exp(-t/\tau_2)$ (Figure 5). The bead luminescence decayed with a major component (71% amplitude) of 0.39 min and a minor component (29% amplitude) of 2.88 min. $R^2$ residuals equaled 0.98 and showed no structure (Figure 5c inset).

**Microscopy set up for Diascopic illumination**: Samples were imaged on an Axiovert 200 inverted microscope equipped for time-resolved imaging. The instrument was modified for diascopic (illumination through the transmitted light path) fluorescence imaging with 280 nm excitation. Light from a xenon flashlamp (Perkin Elmer, FX4401) was filtered (280/20 nm bandpass) and focused onto the back aperture of a quartz condenser (Zeiss, UV KOND, 0.3-0.8 NA). With this configuration, 1-2 μs pulses of light with peak intensities of ca. 150 W $cm^{-2}$ were delivered to the specimen plane. Bright field illumination was achieved through the same condenser assembly by means of a dichroic mirror that passed all light >~350 nm (Semrock, FF347-Di01-25x36). Luminescence was collected through a 540/20 nm emission bandpass filter using a 63X objective lens (EC Plan Neofluar, 63× 1.3 N.A., Carl Zeiss).

For time-resolved imaging of the terbium-labeled sample, the delay between flashlamp excitation and intensifier gate-on was set to 100μs, and the intensifier gate width was 600 μs. The repetition rate of the flashlamp was fixed to 500 Hz, allowing multiple excitation/detection cycles (up to 30) to be implemented during a single 66.6 ms camera frame. A moderate level of intensifier gain was implemented (~700 volts, gain factor = ~5000). Frame summing was implemented with the camera control software to acquire composite images (tagged image file format, .TIF) of four frames (total image acquisition time = 266 ms). Control images (beads w/o $Tb^{3+}$) were not collected as previous experiments revealed no detectable signal.

**2.3 Results**

**Light Source.** We first configured the TRL microscope using a Xe flashlamp as the excitation source. However, this source has a number of limitations, including a long-lived (~100 μs) light that necessitates long gate delay times. We settled on using a UV LED for pulsed, epi-illumination because it offers several performance advantages. First, it has a sub-microsecond fall-time when pulsed, so the gate delay can be reduced to a few microseconds, allowing more efficient signal collection. Second, the repetition rate can be varied over a wider range than the flashlamp (<1 kHz). Although power density is relatively low, the LED pulse width can be modulated to allow for a greater probability of sample excitation. The LED's only disadvantage is that it has a narrow emission wavelength centered at ~ 365 nm, and this limits the range of lanthanide probes that can be excited. For this reason, we used the Xe flashlamp for diascopic illumination of Tb-binding peptides that absorb maximally at 280 nm.

**Objective and coverslip background measurements**: While TRL detection promises complete elimination of short-lived fluorescence, we observed that the optical components in the

excitation light path could be a significant source of long-lived luminescence background. We compared several objectives to determine their background contribution. An ideal objective is one that has adequate UV transmission (~50% at 350 nm), a high NA, and >40X magnification, and very little background. Two oil-immersion objectives, a Zeiss EC Plan Neofluor 63X/1.25 NA and a Partec UV 100X, gave the lowest overall background while meeting the other performance criteria. The full-field, mean pixel gray values for the glass and quartz slide images were 781 and 257, respectively, with gray values approaching detector saturation level in the brightest regions of the glass slide image.

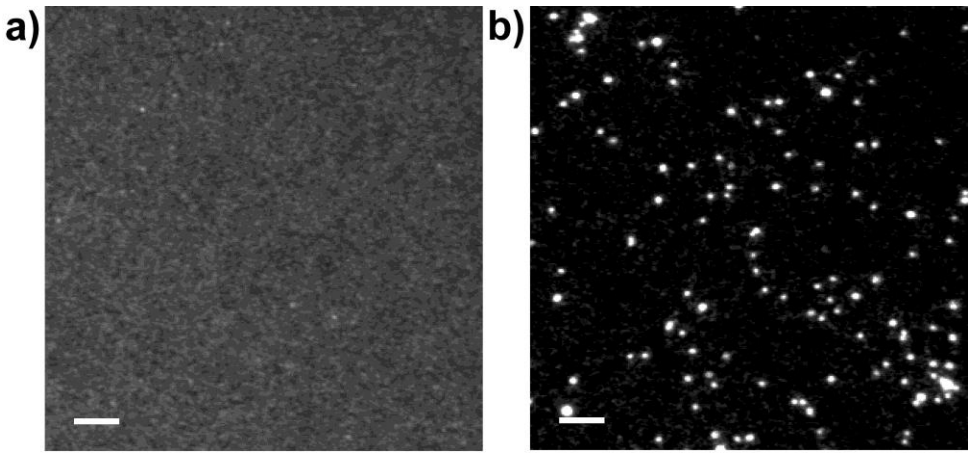


Figure 8: Time-resolved luminescence (TRL) detection eliminates short-lifetime fluorescence background signals. Europium beads (200 nm diameter) were deposited on a quartz coverslip and immersed in a 10 µM solution of AlexaFluor™ 350. The specimen was excited with 365 nm light and emission was viewed through a long-pass (420 nm) filter. (a) In continuous-wave epifluorescence detection mode, the beads cannot be resolved from the fluorescent background. (b) In TRL mode, a short gate delay ($\Delta t$ = 2 µs) between excitation and detection eliminates background and allows clear visualization of single beads (see Materials and Methods and Table 2 for complete image acquisition parameters). Scale bars= 10 µm.

**Evaluation of TRL microscope detection limit and image quality using Eu microspheres.** The instrument's ability to eliminate short-lifetime fluorescence can be clearly seen by comparing images of 200 nm europium beads acquired in continuous-wave fluorescence and TRL detection modes (Figure 8). The beads were deposited on quartz coverslips and immersed in a 10 μM solution of AlexaFluor™ 350. With continuous-wave 365 nm excitation and >420 nm long-pass emission, the europium beads were faintly visible through the eyepiece of the microscope, but the camera could not resolve the beads from background fluorescence of the dye (Figure 8a). By imposing a time delay of only 2 μs between excitation and detection, AlexaFluor™ 350 emission was completely suppressed, and the beads were clearly visible in the TRL image (Figure 8b). The time-resolved image (Figure 8b) shows considerable variability in the brightness of the beads. However, a histogram analysis (see Materials and Methods, Image analysis) revealed distinct regions of intensity corresponding to single beads and clusters of 2 or more beads. The measured net signal intensities of single beads varied ~10% (26,600 ± 2660, mean ± s.d.), and this value is comparable to similar calibration beads developed for time-resolved measurements that have a coefficient of variation of 7 % (70)

TRL image acquisition parameters were optimized to collect the maximum luminescence signal under conditions of sub-saturation illumination intensity (12, 71). Thus, the excitation pulse width and the intensifier gate interval were both set to approximately equal the lifetime of the europium luminescence ($T = T_0 = 600$ μs). The output from 50 excitation pulses (pulse period, $T' = 1300$ μs) was integrated on the CCD within a single camera frame of 66.7 ms (the fastest full-frame readout speed of the camera) at a gain level of ~5,000 (778 V, see Table 2 for complete description of image acquisition and processing parameters for this and other images and data in the chapter). The combination of rapid excitation/detection cycling and emission

signal amplification yielded image acquisition times (66.7 ms) that were 450-fold shorter than those previously reported in a study that imaged similarly sized (107 nm) europium microspheres with a chopper-gated, cooled CCD camera at acquisition times of ~30 s (72).

To evaluate the speed, sensitivity, and precision of our TRL microscope at the limits of detection, we prepared a test specimen consisting of 40 nm, NeutrAvidin-labeled europium beads deposited onto biotinylated quartz coverslips. The beads were reportedly impregnated with a luminescent europium chelate, tris(4,4,4-trifluoro-l-(2-naphthyl)-l,3-butanediono)-bathophenanthroline europium(III) (Invitrogen,Inc., personal communication). To confirm the identity and number of chelates per bead, we prepared the chelate and measured its excitation and emission spectra, quantum yield, and luminescent lifetime, and we compared these values to measurements of the beads. The chelate and beads have identical excitation and emission spectra (Figure 5a) and both exhibit single-exponential luminescence decay kinetics (Figure 5b). We estimated the lifetime of the chelate in toluene to be 450 μs, and the lifetime of the beads was somewhat longer (590 μs), possibly due to the protective effect of the polymer matrix (70). From absorbance measurements of the beads and a measured extinction coefficient of ~45,000 $M^{-1}cm^{-1}$ for the chelate (at $\lambda_{em}$= 350 nm), we estimated that each bead contained, on average, 370 chelate molecules. The luminescent quantum yield of the chelate was measured to be 30% in toluene. Unfortunately, we were unable to accurately determine the quantum yield of the beads. Four separate measurements yielded values ranging from 4 to 15%, with a mean value of 8%.

To evaluate microscope performance, we adapted the methods of Murray et al. to characterize bead images with respect to the number of photons acquired per bead, the image contrast, and the SNR (61). We captured a series of images of the same field of view at different exposure times, numbers of frames and camera gain levels. The pulse/detection timing

parameters were consistent for all images: excitation pulse width (T) = 600 μs; intensifier gate interval ($T_0$) = 600 μs; gate delay (Δt) = 10 μs; and pulse period (T') = 1,300 μs. Frame length could be varied as multiples of the camera frame clock (1 clock = 66.7 ms), and 50 excitation/detection cycles were implemented per frame clock. Therefore, by increasing frame length, exposure time was increased, and more signal was integrated on the CCD sensor before readout. For all measurements, the illumination intensity was held constant at ~0.6 W $cm^{-2}$ at the sample focal plane. Each image yielded 29 individual beads for data analysis.

Figure 9a shows a comparison of photon acquisition efficiency expressed as the average number of photons above the background collected from all single beads in an image as a function of exposure time for three different gain settings. For each image, four frames were summed, and a feature of the image acquisition software that removes random bright spots (saturated pixels resulting from intensifier ion-feedback noise) was implemented. Thus, frame summing had the effect of filtering extreme fluctuations in pixel intensity and reducing the overall variation in pixel background, at the expense of total image acquisition time. The net photons detected per bead was roughly the same for all gain levels within the experimental error, increased proportionally with increasing exposure time and is within the range expected considering the number of molecules per bead, the luminescent lifetime, and the likely detection efficiency of the microscope (see Discussion). The number of photons detected at the longest exposure time (0.90 s, 1,500 excitation/emission cycles) was less than expected (~120 photons per bead detected; ~150 photons per bead expected) based on the observed value at 0.6 s exposure time (~100 photons, Figure 9a). As the chelate in the beads decays biexponentially with a major component of the decay time equal to ~0.4 min (Figure 5c) the repeated exposure of the

same field of view may have diminished the luminescence of the beads, as the images at long exposure times were collected last in the sequence.

To quantify the perceived visibility of single beads, we calculated the ratio of the above-background intensity of each bead to the size of fluctuations in a bead-sized patch of background. The visual impression of the size of a single bead seems limited to about 3 X 3 pixels (Figure 7). This is consistent with a diffraction-limited spot of ~0.25 μm magnified 63X (~16 μm) that overfills the effective pixel size of the detector (~10 μm). Thus, we calculated contrast as $C = S/B^{1/2}$, where B is the sum of the background in a bead-sized patch 3 X 3 pixels, defined as 9b (Eq 8). (Figure 9b) presents the mean contrast for all beads in a single image at each acquisition condition. Contrast appears to increase initially with the number of excitation/emission cycles, and higher gain levels yield higher contrast. While the magnitude of the contrast is somewhat arbitrary, the relative values at different gain levels correlate with the perceived visibility of beads in the images. This can be seen clearly in Figure 10, where single beads are more perceptible in the image taken at the highest gain level.

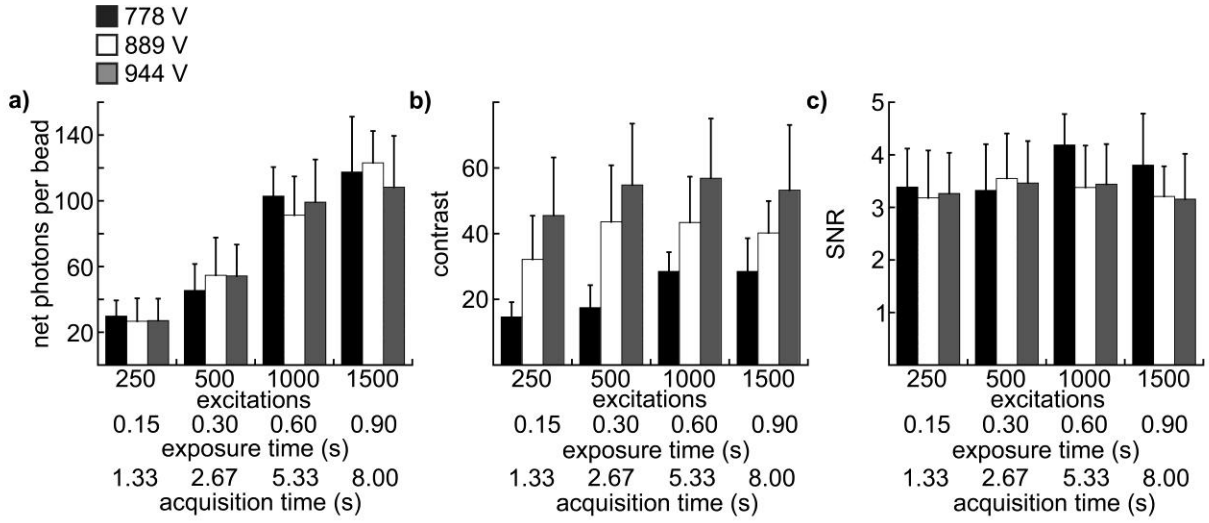


Figure 9: Results of image analyses to determine photon acquisition efficiency, image contrast and instrument precision (SNR). Each chart presents data from 12 individual images collected at 4 different numbers of excitation/emission cycles, exposure times and total acquisition times (indicated on the *x*-axes) and 3 different intensifier gain voltages: 778 V (black columns), 889 V (white columns), 944 V (gray columns). Column height represents the mean value of each parameter (indicated on the *y*-axes) calculated from 29 single beads in a single image, and the error bars represent standard deviation. Source/detector timing parameters and frame summation (four frames summed) were consistent for all images as described in Materials and Methods and Table 1. (a) The net number of photons acquired from a single bead. (b) Contrast. (c) SNR

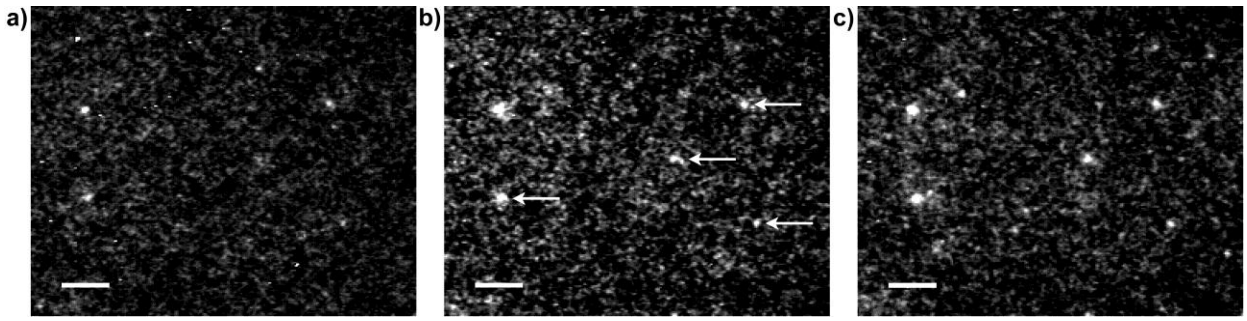


Figure 10: Image contrast increases with intensifier gain level. Images of 40-nm europium beads acquired with 500 excitation/emission cycles and at gain levels of (a) 778 V; (b) 889 V; and (c) 944 V (see Table 1 for complete image acquisition and processing parameters). The arrows in image (b) indicate the location of single beads as verified by histogram analysis and consistent appearance in sequential images (see Materials and Methods, Image Analysis). Other bright spots in the images are either bead clusters or noise artifacts. Scale bars, 10 μm.

While the ability to detect weak signals increases with intensifier gain level, the precision with which faint signals can be measured is the same at all gain levels tested. Precision is indicated by the SNR, which for an image can be represented as the mean signal intensity divided by the error in the signal. Here, we calculated SNR as the net, per-pixel signal intensity from single beads, divided by the standard deviation in local pixel background gray values

$$SNR = \frac{\frac{S}{9}}{\sigma_b}$$ (9(Eq 9). We

then plotted the average value of SNR for all beads in a single image at each acquisition condition (Figure 9c). If the major noise source in the measurements were stochastic fluctuations in the number of photons acquired per bead (Poisson noise), then the SNR should increase in proportion to $S^{1/2}$. However, we observed no increase in SNR at either longer exposure times or higher gain levels (Figure 9c) because the noise measured was far greater than the expected contribution of Poisson noise. The observed trend in SNR is due to the fact that the image intensifier not only amplifies the signal but also adds noise. Each photon entering the image intensifier yields a burst of output photons, and the variation in the gain for each incoming photon and the correlation in time of the output photons contribute to added noise. Furthermore, the intensifier also amplifies background photons that may be present due to residual light from the excitation source, phosphorescence or delayed luminescence from sample or optics or ambient room light (see Discussion section).

We next assessed the instrument's ability to capture high resolution, time-resolved images of living cells that contained a luminescent terbium complex, Lumi4-Tb. Lumi4-Tb is a proprietary analog of a multidentate, 2-hydroxyisophthalamide terbium chelate previously developed by Raymond and coworkers (73). The molecule is brightly luminescent, exhibiting

characteristic terbium emission (Figure 11a) with a quantum yield in water of 0.6 and lifetime of 2.7 ms (manufacturer's specifications). Like most LC's, Lumi4-Tb will not passively diffuse into the interior of living cells from culture medium. Therefore, we used the method of osmotic lysis of pinocytic vesicles to effect delivery of Lumi4-Tb to the cytosoplasm of adherent MDCKII epithelial cells. The pinocytic loading method is well established for delivering macromolecules into the cytoplasm, (74, 75) and we have successfully adapted this method in our laboratory for LC delivery (76). With this method, cells are allowed to undergo pinocytosis in a hypertonic medium containing sucrose, polyethylene glycol and the Lumi4-Tb. Upon transfer to a hypotonic medium, the pinocytic vesicles burst due to the lowering of osmotic pressure, releasing their contents into the cytoplasm. The overall amount of probe molecule delivered into cells can be controlled by varying its concentration in the hypertonic loading medium, or alternatively, by repeated applications of the pinocytosis/lysis process.

Upon cellular delivery, Lumi4-Tb appears to diffuse freely throughout the cytoplasm and nucleus without apparent nonspecific binding, although some of the cells show more brightly luminescent nuclei (Figure 11 b and c). The terbium luminescence is plainly visible when only 110 excitation/emission cycles are integrated within a single camera frame of 333 ms duration (Figure 11b, left); see Table 2 for image acquisition parameters). Image quality is improved when more excitation/ emission cycles (440) are integrated during a single camera frame of 1,333 ms (Figure 11c, left). Image quality is further enhanced by summing four frames at either exposure level (Figure 11 b and c, right). We quantified the differences in observed image quality by calculating the number of photons per pixel, the image contrast, and SNR on a cell-by-cell basis. Increasing the number of excitation/emission cycles proportionally increases the number of photons detected per pixel and the image contrast (Table 3). Frame summing also

increases image contrast, and likewise increases SNR by a factor of ~ 1.5 at either exposure condition (Table 1). Importantly, we visualize Lumi4-Tb luminescence in living cells at total image acquisition times ranging from 0.33 to 5.33 s, suggesting that TRL microscopy, as we have implemented it should be useful for collecting biologically relevant data from live cell specimens (see Discussion section).

**Diascopic Illumination at short wavelengths.** Many luminescent lanthanide complexes, especially terbium complexes, do not absorb light above 350 nm, and therefore cannot be imaged in epi-illumination because internal optics and objective do not transmit in this range. Imperialli and co-workers have engineered $Tb^{3+}$-binding peptides (lanthanide binding tags, or LBTs) that contain a tryptophan residue that absorbs light at ~280 nm and sensitizes $Tb^{3+}$ luminescence. Our lab has established a collaboration with Karen Allen at Boston University. Allen and co-workers have incorporated LBTs into proteins for NMR structural analysis, and they were interested in determining whether $Tb^{3+}$ luminescence from LBT-containing proteins could be imaged microscopically. In order to achieve high-power, 280 nm UV excitation, we configured the TRL microscope for diascopic illumination using a Xe flashlamp source. With this configuration, we successfully imaged $Tb^{3+}$ luminescence from glutathione-sepharose beads that were bound to a fusion protein consisting of glutathione-s-transferase linked to LBT-modified, interleukin 1β (GST-IL1β-S1-$Tb^{3+}$). Preliminary imaging results showed that $Tb^{3+}$ luminescence was detectable with only a single pulse/detection cycle, indicating that the samples were very bright. With 5 pulse/detection cycles integrated, the detector was mostly saturated (Figure 12). While these samples contained an extremely high protein density (~$10^6$ proteins/bead), the ability to image these samples in TRL mode suggests the possibility of studying cell-surface receptors that have been labeled with LBTs.

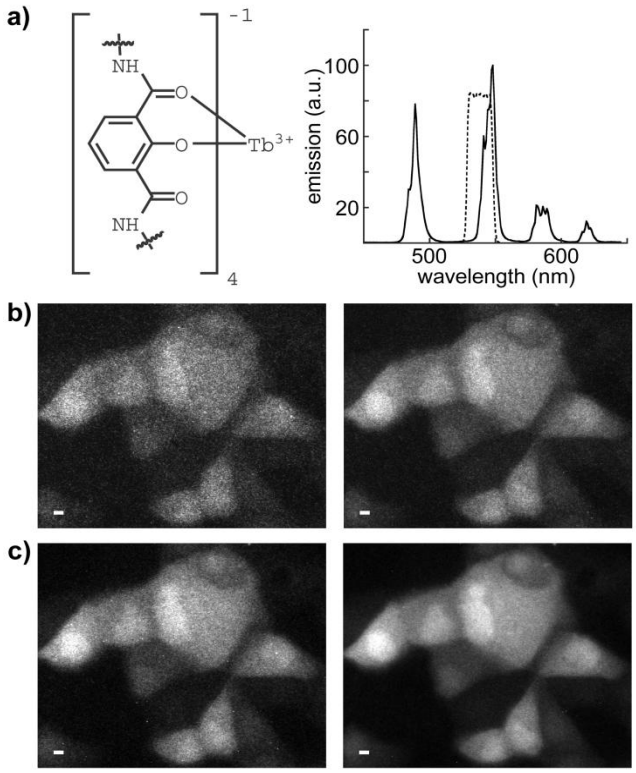


Figure 11: Visualization of a luminescent terbium complex in living cells with time-resolved microscopy. Image quality is enhanced by increasing exposure time and summing multiple frames to generate a single image. (a) left, partial structural representation of Lumi4-Tb, a proprietary analog of a multidentate, 2-hydroxyisophthalamide terbium chelate reported by Raymond and coworkers; (46) right, characteristic terbium emission spectrum of Lumi4-Tb. The compound emits with a quantum yield of _0.6 and a lifetime of _2.7 ms. A narrow-pass filter (transmittance shown as dotted lines) captures _35% of the total terbium emission. (b,c) Time-resolved luminescence micrographs showing MDCKII cells that were loaded with Lumi4-Tb by osmotic lysis of pinocytic vesicles (see Materials and Methods). Complete details of data collection and image processing parameters are provided in Table 1. Scale bars, 10 lm. (b) Images of 110 excitation/emission cycles (exposure time 5 165 ms). Left, single frame; right, four frames summed. (c) Images of 440 excitation/emission cycles (exposure time 5 660 ms). Left, single frame; right, four frames summed.

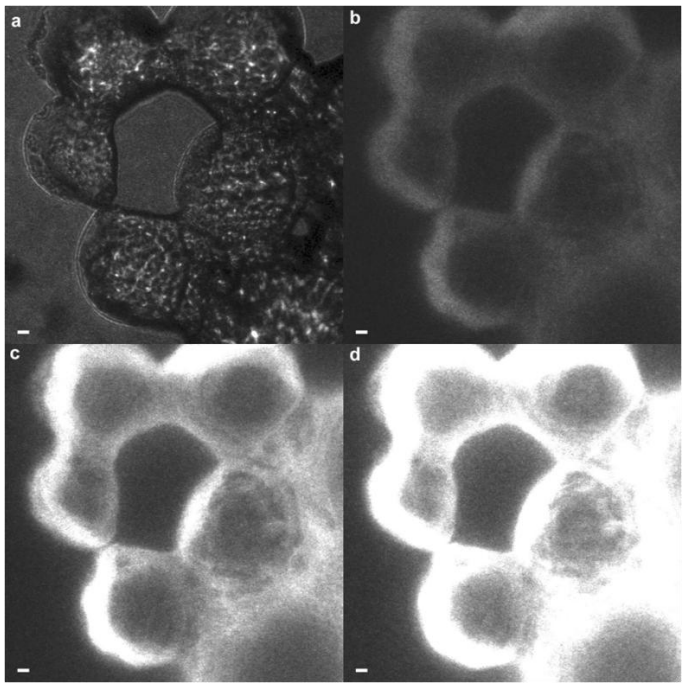


Figure 12: Brightfield (a) and time-resolved (b-d) images of sample (beads in IL1b buffer + 150 nmol GST-IL1b-S1-$Tb^{3+}$)**.** Time-resolved images were acquired as described in text: (b) 1 excitation/detection cycle; (c) 3 excitation/detection cycles (d) 5 excitation/detection cycles. Images were rendered at identical contrast levels. Scale bars 10 μm.

## 2.4 Discussion

The well established benefits of TRL detection in cell-free bioassays have motivated considerable efforts to develop LCs and other long-lived probes for cellular imaging applications (5, 8, 76-80). Underlying these efforts is an assumption that autofluorescence background elimination will considerably enhance the sensitivity of cellular imaging relative to that routinely observed with steady-state detection of short-lifetime fluorescent proteins or organic fluorophores. However, it is worthwhile to consider that live cell imaging requires adequate photon acquisition from a limited number of luminescent species. For example, over-expressed fluorescent proteins are typically imaged in mammalian cells at concentrations of 1–10 μM (ca. 106–107 copies per typical cell of 1–2 pL volume)(81). Similarly, fluorescent indicators used to

image analyte concentration (e.g., $Ca^{2+}$, $Zn^{2+}$) are preferably loaded into cells at ~10–20 μM concentration (82). These cellular concentration levels reflect a need to balance detectability with minimal perturbation of physiological function. Assuming a diffuse cellular distribution, a diffraction limited volume element (~1 fL) may contain <1,000 fluorescent molecules. Furthermore, exposure times are limited by the need to resolve dynamic biological processes and to limit photobleaching of probes and photodamage to cells. Given these constraints, a primary motivation of this work was to explore the limits of sensitivity and time resolution that can be achieved with TRL microscopy of long-lifetime LC probes.

The number of photons detected from a single lanthanide specimen is dependent on the number of molecules in the illumination volume, the efficiency with which those molecules are excited, and the photon collection efficiency of the time-resolved detection system (83-84) (85) (86). For our microscope system, the probability of exciting a single europium chelate molecule can be estimated using the following equation (83) (85):

$$E_{ex} = 2.303X10^{3}\,\frac{\varepsilon\lambda_{ex}I_{ex}T}{N_{A}hc} \qquad (10)$$

where ε is the extinction coefficient of the europium chelate at the excitation wavelength (~40,000 $M^{-1}cm^{-1}$), $\lambda_{ex}$ is the wavelength of excitation light (365 X $10^{-7}$ cm), $I_{ex}$ is the intensity of illumination at the sample plane (0.6 W $cm^{-2}$), T is the excitation pulse width (600 μs), $N_A$ is Avogadro's number; h is Planck's constant, and c is the speed of light. Thus, the probability that a single pulse excites a europium chelate molecule embedded in a bead is ~0.10.

With time-resolved detection, the width of the intensifier gate window $T_0$ (600 μs) after time-delay, Δt (10 μs) permits a certain proportion $E_{TRL}$ of the decaying luminescence emission from the probe molecules to be collected as given by (83, 85):

$$E_{TRL} = e^{-\Delta t/\tau}(1 - e^{-T_0/\tau}) \quad (11)$$

where τ is the luminescent lifetime of the chelate (590 μs), yielding in this case a maximum proportion of detectable luminescence equal to ~0.63. The probability that a photon absorbed by the chelate will yield a detectable emission photon is then given by:

$$E_{em} = QY.E.QE.E_{TRL} \quad (12)$$

where QY is the quantum yield of the chelate in the beads (0.08), E is the light collection efficiency of the microscope (estimated to be 15% for our system), and QE is the quantum efficiency of the intensifier at the wavelength of emission (0.38), and $E_{em}$ equals ~2.9 X $10^{-3}$ for detecting a photon emitted from a europium bead with our TRL microscope. The expected number of photons detected from a single, 40-nm bead is then simply equal to:

$$N = n.N_{ex}.E_{ex}.E_{em} \quad (13)$$

where n is the number of europium chelates per bead (~370), and $N_{ex}$ is the number of excitation/emission cycles implemented in a single camera exposure. For the case where $N_{ex}$ is 500, N equals ~54, and the measured values ranged from 45 to 55 under these conditions (Figure 9c), in excellent agreement with the calculation.

We evaluated performance in terms of photon detection efficiency, image contrast, and SNR. The relative importance of any one of these factors will ultimately be dictated by the needs

of a particular application. For example, if the goal is to detect faint signals, the best performance is achieved by operating the camera at high gain levels. However, if precise quantification of luminescence is required, no enhancement in SNR is realized by imaging at high gain or by increasing the number of excitation/emission events beyond that needed to achieve adequate image contrast. In all cases, frame summing will improve the SNR at the expense of overall image acquisition time. We observed that the SNR is lower than that expected based on the photon counts at all gain levels measured.

One factor that may contribute to suboptimal SNR is the presence of a significant background signal that we attribute to phosphorescence from the microscope objective itself. The observed signal level was striking when we acquired TRL images of clean glass and quartz microscope slides through a long-pass emission filter ($\lambda > 420$ nm). The slide images were acquired using the same timing parameters as for the bead images, a gain level of 778 V and a single camera frame of 666 ms during which 500 excitations were implemented (10-bit image, pixel depth = 1,024). The full-field, mean pixel gray values for the glass and quartz slide images were 781 and 257, respectively, with gray values approaching detector saturation level in the brightest regions of the glass slide image. The mean gray value observed without any slide or immersion oil on the objective was similar to the level observed with clean quartz slides. Much of the background signal in bead test specimens (measured on quartz substrates) was filtered out by capturing europium emission through a narrow pass filter, however a residual component was still present that added noise to the images.

While Connally and coworkers have shown that commercial UV LED's emit a weak, long-lifetime visible light signal, (13-14) we rule this out as a substantial source of non-specific background for three reasons: (1) the excitation and emission filters should effectively remove

any visible component (for filter details, see Materials and Methods, Data Collection); (2) the observed signal level with no objective in the light path is negligible (i.e., effectively attenuated by the excitation filter); and (3) different objective lenses result in varying levels of observed signal. Imaging quality microscope objectives are constructed from multiple glass lenses of varying composition that are often coated with thin, antireflective films. Therefore, practical implementation of TRL microscopy requires careful selection of objective lenses that exhibit minimal phosphorescence.

In live-cell imaging experiments, we observed that it was possible to visualize a luminescent terbium complex, Lumi4- Tb, diffusely distributed throughout MDCKII cells within image acquisition times as short as 333 ms. By increasing the number of excitation/emission cycles and/or summing multiple frames, the overall quality of cell images was improved (as measured by image contrast and SNR) at the expense of increased acquisition times (Figure 11 b and c; Table 2 and Table 3). Furthermore, we note that the cell images presented here were captured at a moderate intensifier gain voltage (778 V, gain factor = 5,000); increasing the gain improves sensitivity, and thus shortens image acquisition time, at the expense of noisier images. Given a natural rate of pinocytosis of ~3 X $10^{-16}$ $Lmin^{-1}$ for most cell types, (75) assuming typical cell volumes of 1–2 pL, the estimated cellular concentration of Lumi4-Tb was ~300 nM for the experimental conditions used in this study (single loading application, 200 µM Lumi4-Tb, 10 min pinocytosis, see Materials and Methods). This concentration is considerably lower than the cellular concentrations of fluorescent proteins or conventional fluorophores that are typically observed in live-cell imaging experiments (~10 µM) (81-82).

Our results show that high resolution, quantitative TRL microscopy can be performed on a conventional epi-fluorescence microscope using commercially available light sources and

detectors. The system we developed can image a few hundred LC probe molecules localized to a diffraction-limited spot within ~1-s time intervals and can be used to image lanthanide luminescence in living cells at submicromolar cellular concentrations. While the measured performance characteristics should be adequate for a number of live cell imaging applications, even greater sensitivity and precision could be attained by using more sensitive ICCD cameras that are capable of single photon counting. Further improvements could be realized by using shorter, more intense excitation pulses (e.g., from pulsed lasers) that would saturate probe absorption and allow for more efficient photon collection, and by minimizing phosphorescence background from microscope objectives. Thus, we conclude that practical, live-cell TRL imaging is readily achievable with current optical technologies. Ongoing efforts to develop more brightly luminescent LC's, nanoparticles, and other long-lifetime probes, including europium species that can be excited with visible light should lead to further improvements in detectability (6, 77-78, 87-91). Methods to deliver such probes to the interior of living cells and target them to selected macromolecules or sub-cellular structures should benefit a variety of live-cell imaging experiments where non-specific fluorescence background is particularly problematic (76, 79).

# Chapter 3

# PROBE DEVELOPMENT FOR CORRELATED LUMINESCENCE AND ELECTRON MICROSCOPY

## 3.1 Introduction

PAMAM dendrimers are versatile nanostructures that offer several features which can be leveraged to design useful biological probes. The terminal surface amines can be functionalized with multiple fluorophores or other groups. Cystamine core, PAMAM denrimers can be reduced, presenting a single thiol that can be coupled to a targeting ligand. Finally, it has been shown that the tertiary amines in the dendrimer core can serve as nucleation points to reduce metal ions and template the growth of small (~nm) metal particles. We sought to leverage the unique characteristics of PAMAM dendrimers to design protein-targeted probe molecules that possess one or more of the above-mentioned characteristics.

Initially, our aim was to label a single dendrimer with multiple fluorophores or luminescent lanthanide complexes as a means to increase overall emission. By also labeling the dendrimer with a ligand like biotin or trimethoprim (TMP), we hypothesized that we could target it to a specific protein. Biotin functionalization allows targeting to streptavidin, while TMP binds selectively and stably (~1 nM $K_D$) to *Escherichia coli* dihydrofolate reductase (eDHFR). Over-expressed eDHFR fusion proteins can be selectively labeled with TMP conjugates in cell lysates or living cells, and we assumed this strategy could be applied using TMP-dendrimer conjugates (76, 92-94).

When designing a protein-targeted probe for cell-based applications, it is desirable that the probe have only one targeting ligand; in other words, the probe should be monovalently functionalized. Multivalent probes that have more than one targeting ligand can lead to protein dimerization or oligomerization. To achieve monovalent functionalization, we developed a synthetic protocol where cystamine core PAMAM dendrimers were first labeled multivalently

with fluorophores, then subsequently reduced to obtain two dendrons with exactly half the molecular weight of the original dendrimer. The dendrons each possess a single sulfhydryl group that serves as a point of attachment for monovalent linkage to thiol-reactive biotin or TMP.

Another property of PAMAM that we sought to exploit for probe development is their ability to encapsulate and stabilize metal and semiconductor nanoparticles. Gold nanoparticles 1 -3 nm in diameter have been shown to be effectively encapsulated inside dendrimers of generation 4 (G4) and higher (95). Gold particles can serve as contrast agents for electron microscopy (EM) due to their high electron density. In this application, gold nanoparticles are typically conjugated to secondary antibodies, which are then used to label samples that have been first labeled with a specific, primary antibody. The drawback of this approach is that the large size of the targeting antibodies yield a relatively low labeling density, and this reduces the resolution seen in the microscope image (38). We hypothesized that monovalent, TMP-functionalized dendrons that encapsulate a nanoparticle could perhaps be targeted to eDHFR fusion proteins in fixed cells in a way that yields high labeling density. This strategy might, in turn, enable high-resolution, EM imaging of protein complexes.

While ligand-functionalized gold nanoparticles based probes are commercially available, they typically present multiple ligands, or are, at best, only 80 % monovalent (36, 96). Indeed, monovalent functionalization of nanoparticles in general presents a considerable challenge, and only a few strategies have been reported. For example, Ting and co-workers presented a strategy to prepare monovalent CdSe nanoparticles that required initial linkage to DNA, and subsequent, low-yield electrophoretic purification to yield particles with a single point of attachment (97). We sought to determine whether monovalently functionalized PAMAM dendrons could serve as

templates for gold nanoparticle synthesis, thus providing a general strategy for monovalent nanoparticle functionalization as well as a potential EM imaging probe. We further sought to determine whether ligand-dendron-gold structures could be further labeled with fluorophores, thereby producing a multifunctional structure that could be used for correlated fluorescence and EM imaging applications.

In this chapter, the synthetic strategies for functionalizing cystamine core G4 and G5 PAMAM dendrimers as well as templating nanoparticle growth are presented. The general strategy entailed 1) amide bond linkage of fluorophores to surface amines; 2) passivation of remaining amines with hydroxyl or acetyl groups to yield electrostatically neutral structures; 3) reduction and subsequent reaction with maleimide- or iodide-functionalized ligands; and 4) gold particle templating. Products were characterized using NMR, UV-Vis, TEM, and ligand-binding assays to assess monovalency, the ability to bind protein targets, the for attaching the fluorophore and ligand and for encapsulating the gold nanoparticle. We explored Lumi4 and TAMRA as the probes.

## 3.2 Materials and Methods

### 3.2.1 Materials:

Cystamine core PAMAM dendrimers (Generations 4 and 5) were purchased from Dendritic Nanotechnologies, Inc. All chemicals were obtained from Sigma Aldrich, Inc. (Milwaukee, WI). TEM images were obtained on a JEOL JEM-3010 conventional TEM. High performance liquid chromatography (HPLC) was performed on a Beckman System Gold with a C18 column (GraceVydac, cat. no. 218TP54, 5 μm, 4.6 mm i.d. x 250 mm). LRET Binding assays were done using a multi-well plate reader capable of time-gated luminescence detection

(Perkin-Elmer, Victor 3 V). Centrifugal concentrators (molecular weight cut-off, MWCO = 3000 Da) were purchased from Millipore, Inc. MALDI-TOF mass spectra was performed on an Applied Biosystems Voyager-DE STR at the University of Illinois-Urbana Dept. of Chemistry. Low-resolution electrospray (ESI) mass spectra were obtained at the UIC Research Resources Center (RRC). UV-Vis absorption spectra were recorded using a Cary 3000 spectrophotometer (Varian, Inc.). Fluorescence emission spectra were recorded using a Fluoromax 3 fluorimeter (Horiba–Jobin Yvon, Inc.).

### 3.2.2 Synthesis

#### 3.2.2.1 G4-OH (69), Scheme 1

Glycidol (128 eq) was added to a solution of cystamine core G4 (1.02μmol) in 1 mL methanol and the solution was stirred at 40$^{o}$C for 2 days. Methanol was evaporated and the mixture was dissolved in water. The product was purified by centrifugation using a filter device with a MWCO of 3000. MALDI and NMR were used to confirm product. $^{1}$H NMR (500 MHz, $D_2O$) δ 2.37 (248 H, br), 2.58 (120 H br), 2.79 ( 368 H, br), 3.3 ( 248 H, br), 3.78(1 H, br). MALDI-TOF MS: calc. for $C_{909}H_{1918}N_{250}O_{314}S_2$ $[M+H]^+$: 21414 Da, found: 20,400 Da.

#### 3.2.2.2 G4-Ac(2), G5-Ac(3), Scheme 2

100 eq triethylamine (200 eq for cys G5) was added to a solution of 2.79 μmol cysG4 (1.73 μmol cys G5) in 8 mL methanol under $N_2$ at RT. This was followed by the addition of 100 eq acetic anhydride (200 eq for cys G5). The solution was stirred for 2 days. Methanol was evaporated and the mixture dissolved in water. The product was purified by centrifugation (MWCO of 3000). MALDI and NMR were used to confirm product $^{1}$H NMR (500 MHz, $D_2O$) for G4-Ac: δ 1.84 (3 H, s), 2.37 (248 H, br), 2.58 (120 H br), 2.79 ( 368 H, br), 3.3 ( 248 H, br). MALDI-TOF MS: calc. for $C_{752}H_{1381}N_{250}O_{188}S_2$ $[M+H]^+$, 16977 Da, found: 16,330 Da. $^{1}$H

NMR (500 MHz, $D_2O$) for G5-Ac: δ 1.84 (3 H, s), 2.34 (504 H, br), 2.58 (248 H br), 2.79 ( 760 H, br), 3.3 (504 H, br). MALDI-TOF MS: calc. for $C_{1520}H_{2789}N_{506}O_{380}S_2$ $[M+H]^+$, 34256 Da, found: 31,594 Da.

**Scheme 1:**

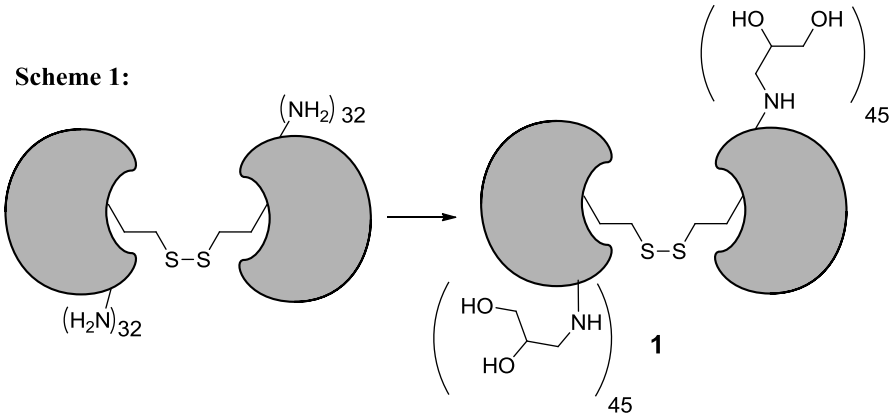


Reaction: i) glycidol, MeOH

**Scheme 2:**

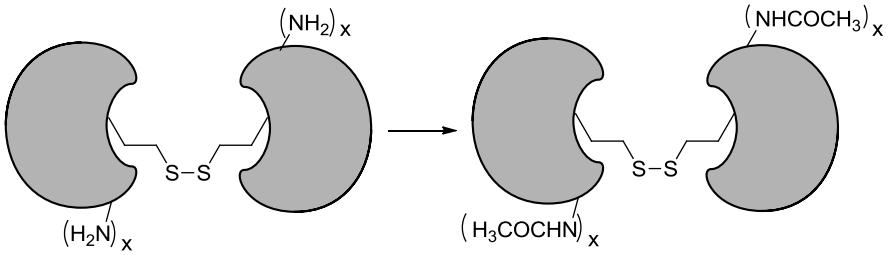


**2(G4-Ac), 3(G5-Ac)**

Reaction: Acetic anhydride, TEA, MeOH
x= 32 for cysG4, 64 for cysG5

**3.2.2.3 TMP-OH (4), Scheme 3.**

60 mL 48% HBr was preheated to ~100°C in a round-bottom flask with a magnetic stir-bar. While stirring, 5.00 g trimethoprim (17.4 mmol) was added and stirred for 20 min. The reaction was quenched by slow, drop-wise addition of 15 mL 50% NaOH. After the reaction cooled to room temperature, the flask was chilled in an ice-water bath for 4 h, allowing crystals to form. Crystals were filtered using a vacuum flask apparatus and wash with ca. 10 mL ice-cold water. Crystals were collected and dissolved in 75-100 mL boiling water. The pH of the solution was adjusted to pH = 7 using $NH_4OH$ (30% w/w), and stored at 4°C overnight, leading to recrystalization. Crystals were filtered and dried under vacuum, yielding compound 4 (2.75 g, 10.0 mmol, 58%) $^1$H NMR (500 MHz, [D4] $CH_3OH$): δ = 7.51 (1 H, s), 6.63 (2 H, s), 3.85 (6 H, s), 3.65 (2 H, s).

**3.2.2.4 TMP-I (5), Scheme 3.**

TMP-OH (1.8mmol) and potassium tert.butoxide (1.1 eq) were dried under vacuum for an hour. The two were separately dissolved in 5mL DMSO each under $N_2$ at RT and then mixed. 1,6 diiodohexane (5 eq) was added and stirred for 3 hours. 20 mL $H_2O$ was added to the mixture. The mixture was extracted (3x 50mL ethyl acetate) and the extractions were washed with water. The organic layer was dried with $MgSO_4$, filtered and concentrated under reduced pressure. The resulting product was adsorbed onto silica and subjected to flash chromatography, 7% MeOH in DCM, to obtain pure compound **5**. $^1$H NMR (500 MHz, [D4] $CH_3OH$): δ = 7.45 (1 H s), 6.52 (2 H s), 3.90 (2 H, t), 3.78 (6 H s), 3.63 (2H s), 1.82 (2 H, m), 1.68 (2 H m), 1.48 (4 H, m). ESI-MS, TMP-I ($C_{19}H_{27}IN_4O_3$): m/z 487 $[M+H]^+$ .

**Scheme 3:**

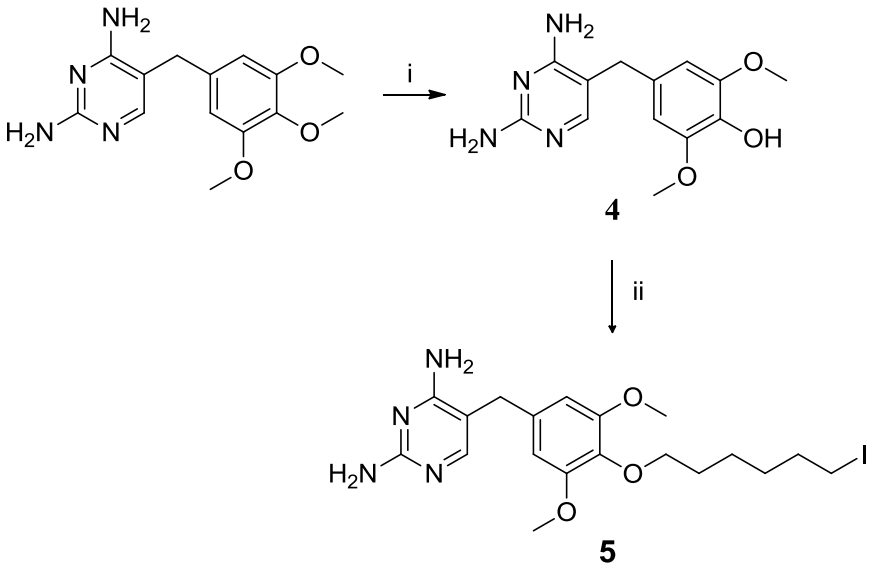


Reagents: i) HBR ii) 1,6 diiodohexane, pot tert butoxide, DMSO

**Scheme 4:**

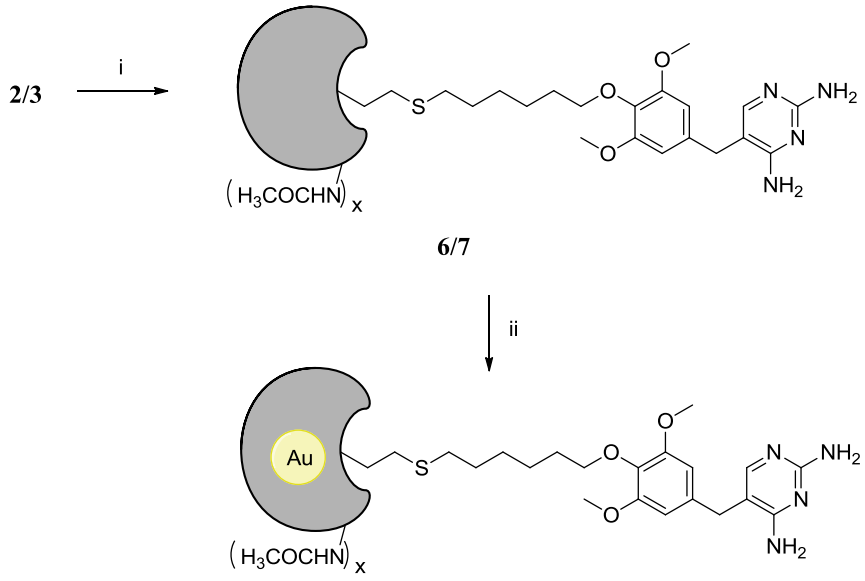


Reaction: i) TCEP.HCl, $H_2O$; TMP-I, NaOMe, DMF ii) $HAuCL_4$, $NaBH_4$ in 0.3M NaOH.
X= 32 for cysG4, 64 for cysG5.

**3.2.2.5 G4-Ac-TMP (6), Scheme 4.**

0.618 µmol of G4-Ac was dissolved in 1.5 mL of $H_2O$. To this 814 µL of 3.5mM TCEP.HCl was added. This was stirred for 2 hours. The water was evaporated and the mixture was dissolved in 2 mL DMSO. To this mixture 3eq TMP-I and 10µL of freshly prepared 1M NaOMe solution was added and stirred overnight under $N_2$ at RT. The solution was diluted in 30 mL $H_2O$ and purified by centrifugation using a filter device with a MWCO of 3000. MALDI, NMR and an SDS gel were used to confirm product. $^1$H NMR (500 MHz, D2O) for G4-Ac-TMP: δ 1.84 (3 H, s), 2.37 (248 H, br), 2.58 (120 H br), 2.79 ( 368 H, br), 3.3 ( 248 H, br), 6.5 (2H s), 7.5 (1H s). G4-Ac-TMP was purified with by reverse-phase HPLC (5 min linear gradient, from 0% to 95% solvent B, 95% B constant for 15 mins, 5 min linear gradient from 95% to 0% solvent B(solvent A, 0.1 M triethylammonium acetate (pH 6.5) plus 5% $CH_3CN$; solvent B, acetonitrile)). MALDI-TOF MS: calc. for $C_{395}H_{718}N_{129}O_{97}S$ $[M+H]^+$, 8847 Da, found: 8432 Da.

**3.2.2.6 G5-Ac-TMP (7), Scheme 4.**

The same procedure was used as for **6**. The product was purified by size exclusion chromatograpy using a Sephadex G-75 gel and 1 mM $K_2HPO4$, pH = 7.4 as the solvent. Product was confirmed using NMR, MALDI and SDS-PAGE. $^1$H NMR (500 MHz, $D_2O$) for G5-Ac-TMP: δ 1.84 (3 H, s), 2.34 (504 H, br), 2.58 (248 H br), 2.79 ( 760 H, br), 3.3 ( 504 H, br), 6.5 (2H s), 7.5 (1H s).MALDI-TOF MS: calc. for $C_{779}H_{1422}N_{257}O_{193}S_1$ $[M+H]^+$, 17487 Da, found: 16262 Da.

### 3.2.2.7 G4-OH-Biotin (8), Scheme 5

1 µmol G4-OH (69) was dissolved in 50 mM HEPES, pH 7. 1 mL TCEP gel was added and the reaction stirred for 2 hours. The gel was centrifuged out, and 7 eq N-Biotinoyl-N'-(6-maleimidohexanoyl)hydrazide (biotin maleimide) dissolved in 200 µL DMSO was added. The reaction was stirred overnight. The product was purified by centrifugation using a filter device with a MWCO of 3000. Product was confirmed using NMR, MALDI and SDS-PAGE. $^{1}$H NMR (500 MHz, $D_2O$) for G4-OH-Biotin: δ 1.5 (2 H m), 1.6 (4 H m), 1.7 (2 H m), 2.37 (248 H, br), 2.58 (120 H br), 2.79 ( 368 H, br), 3.3 ( 248 H, br), 3.78(1 H, br). MALDI-TOF MS: calc. for $C_{474.5}H_{989.5}N_{130}O_{162}S_2$ $[M+H]^+$, 11160 Da, found: 10,000 Da.

**Scheme 5:**

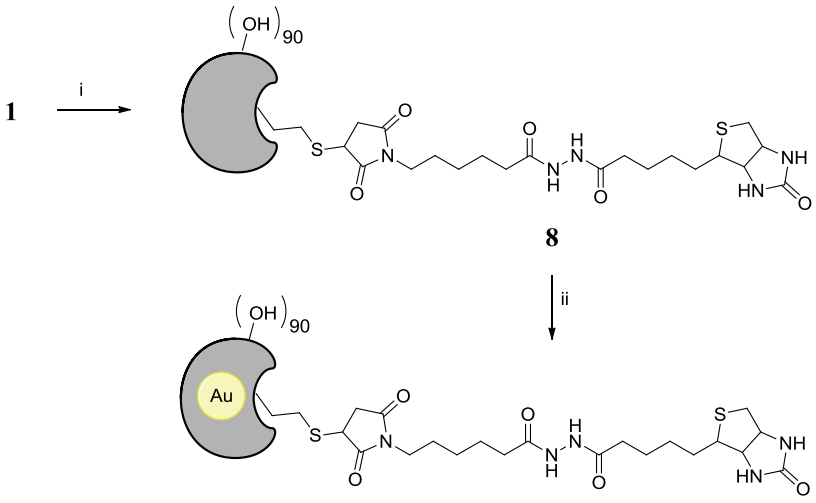


Reaction: i) TCEP gel, HEPES, N-Biotinoyl-N'-(6-maleimidohexanoyl)hydrazide,DMSO iii) $HAuCl_4$, $NaBH_4$ in 0.3M NaOH

### 3.2.2.8 G4-TAMRA (9), Scheme 6

1.68 µmol cysG4 was dissolved in 1 mL DMF. To this 6.25 eq TAMRA, 6.25 eq HBTU, 6.25 eq HOBT and 15 eq TEA was added. The reaction was stirred overnight under $N_2$ at RT. The solution was diluted in 30 mL $H_2O$ and purified by centrifugation using a filter device with a MWCO of 3000. MALDI, NMR and UV-Vis were used to confirm product. $^1$H NMR (500 MHz, $D_2O$) for G4-TAMRA: δ 2.37 (248 H, br), 2.58 (120 H, br), 2.79 (368 H, br), 3.3 (248 H, br), 6.27 (2 H, br), 6.67 (2 H, br), 7.02 (2 H, br), 7.91 (1 H, br), 8.02 (1 H, br), 8.26 (1 H, br). MALDI-TOF MS: calc. for $C_{674}H_{1294}N_{254}O_{132}S_2$ $[M+H]^+$, 15114 Da, found: 14330 Da.

### 3.2.2.9 G4-TAMRA-OH (10), Scheme 6

14 mg **9** was dissolved in methanol and 7.5 µL glycidol was added. The reaction was stirred at 40$^o$C for 2 days. Methanol was evaporated and the mixture was dissolved in water. The product was purified by centrifugation using a filter device with a MWCO of 3000 and directly used for the next step. NMR and UV-Vis were used to confirm product $^1$H NMR (500 MHz, $D_2O$) for G4-TAMRA-OH: δ 2.37 (248 H, br), 2.58 (120 H br), 2.79 ( 368 H, br), 3.3 ( 248 H, br), 3.78(1 H, br) , 6.39 (2 H, br), 6.75 (2H, br), 7.05 (2H, br), 7.92 (1H, br), 8.04 (1H, br), 8.26 (1H, br).

### 3.2.2.10 G4-TAMRA-OH-Biotin (11), Scheme 6.

11 mg **10** was dissolved in 2 mL 50mM HEPES. To this 1 mL TCEP gel was added and the reaction stirred for 2 hours. The gel was centrifuged out, and 1mg N-biotinoyl-N'-(6-maleimidohexanoyl)hydrazide (biotin maleimide) dissolved in 200 µL DMSO was added. The reaction was stirred overnight. The product was purified by centrifugation using a filter device with a MWCO of 3000. Product was confirmed using NMR, MALDI, UV-Vis and SDS-PAGE. $^1$H NMR (500 MHz, $D_2O$) of G4-TAMRA-OH-Biotin: δ 1.3 (2H m), 1.5-1.7 (6H br), 2.37 (248

H, br), 2.58 (120 H br), 2.79  368 H, br), 3.3 (248 H, br), 3.78(1 H, br) 6.41 (2 H, br), 7.05 (2H, br), 7.92 (1H, br), 8.26 (1H, br).MALDI-TOF MS: calc. for $C_{474.5}H_{930}N_{132}O_{142}S_2$ $[M+H]^+$, 10597 Da, found: 10833 Da.

**Scheme 6:**

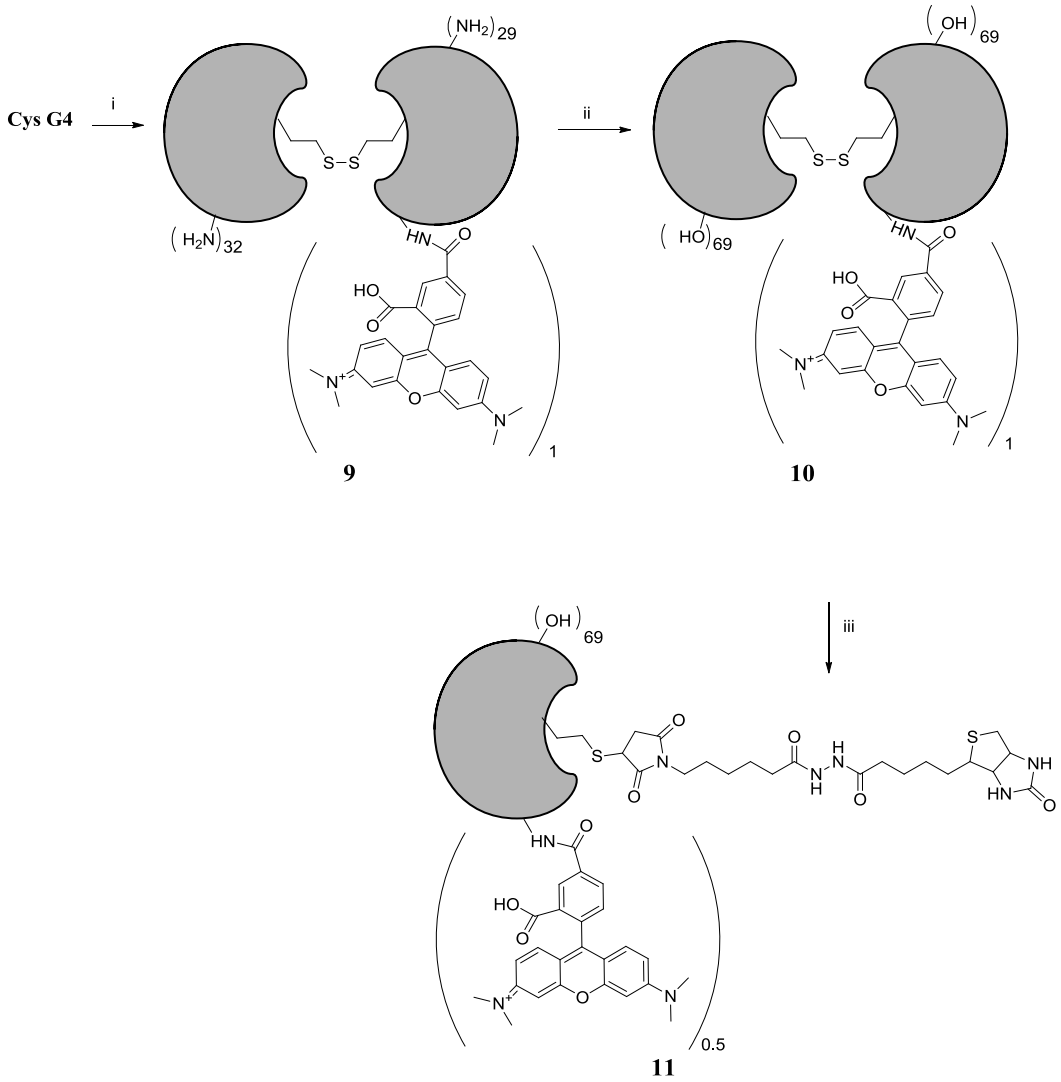


Reaction: i) TAMRA, HBTU, HOBT, TEA, DMF ii) Gylcidol, MeOH iii) TCEP gel, HEPES, N-Biotinoyl-N'-(6-maleimidohexanoyl)hydrazide,DMSO

### 3.2.2.11 G5-TAMRA (12), Scheme 7

1 µmol cysG4 was dissolved in 1 mL DMF. To this 10 eq TAMRA, 10 eq HBTU, 10 eq HOBT and 15 eq TEA was added. The reaction was stirred overnight under $N_2$ at RT. The

solution was diluted in 30 mL $H_2O$ and purified by centrifugation using a filter device with a MWCO of 3000. The product was directly used for the next step.

### 3.2.2.12 G5-TAMRA-Ac (13), Scheme 7

200 eq triethylamine was added to a solution of 1µmol cysG5 in 8 mL methanol under $N_2$ at RT. This was followed by the addition of 200 eq acetic anhydride. The solution was stirred for 2 days. Methanol was evaporated and the mixture dissolved in water. The product was purified by centrifugation using a filter device with a MWCO of 3000. $^1$H NMR (500 MHz, $D_2O$) for G5-TAMRA-Ac: δ 1.84 (3 H, s), 2.34 (504 H, br), 2.58 (248 H br), 2.79 ( 760 H, br), 3.3 ( 504 H, br), 6.41 (2 H, br), 6.73 (2H, br), 7.07 (2H, br), 7.32 (1H, br), 7.92 (1H, br), 8.19 (1H, br). MALDI-TOF MS: calc. For $C_{1681}H_{2921}N_{520}O_{401}S_2$ $[M+H]^+$, 36853 Da, found: 36878 Da.

### 3.2.2.13 G5-TAMRA-Ac-TMP (14), Scheme 7

0.618 µmol of G5-TAMRA-Ac was dissolved in 1.5 mL of $H_2O$. To this 814 µL of 3.5mM TCEP.HCl was added. This was stirred for 2 hours. The water was evaporated and the mixture was dissolved in 2 mL DMSO. To this mixture 3eq TMP-I and 10µL of freshly prepared 1M NaOMe solution was added and stirred overnight under $N_2$ at RT. The product was purified by centrifugation using a filter device with a MWCO of 3000. Product was confirmed using NMR, UV-Vis, MALDI and SDS-PAGE. $^1$H NMR (500 MHz, $D_2O$) for G5-TAMRA-Ac-TMP: δ 1.84 (3 H, s), 2.34 (504 H, br), 2.58 (248 H br), 2.79 ( 760 H, br), 3.3 (504 H, br), 6.41 (2 H, br), 6.73 (2H, br), 7.07 (2H, br), 7.32 (1H, br), 7.92 (1H, br), 8.19 (1H, br). MALDI-TOF MS: calc. For $C_{859.5}H_{1487.5}N_{264}O_{203.5}S$ $[M+H]^+$, 18785.5 Da, found: 18837 Da.

**Scheme 7:**

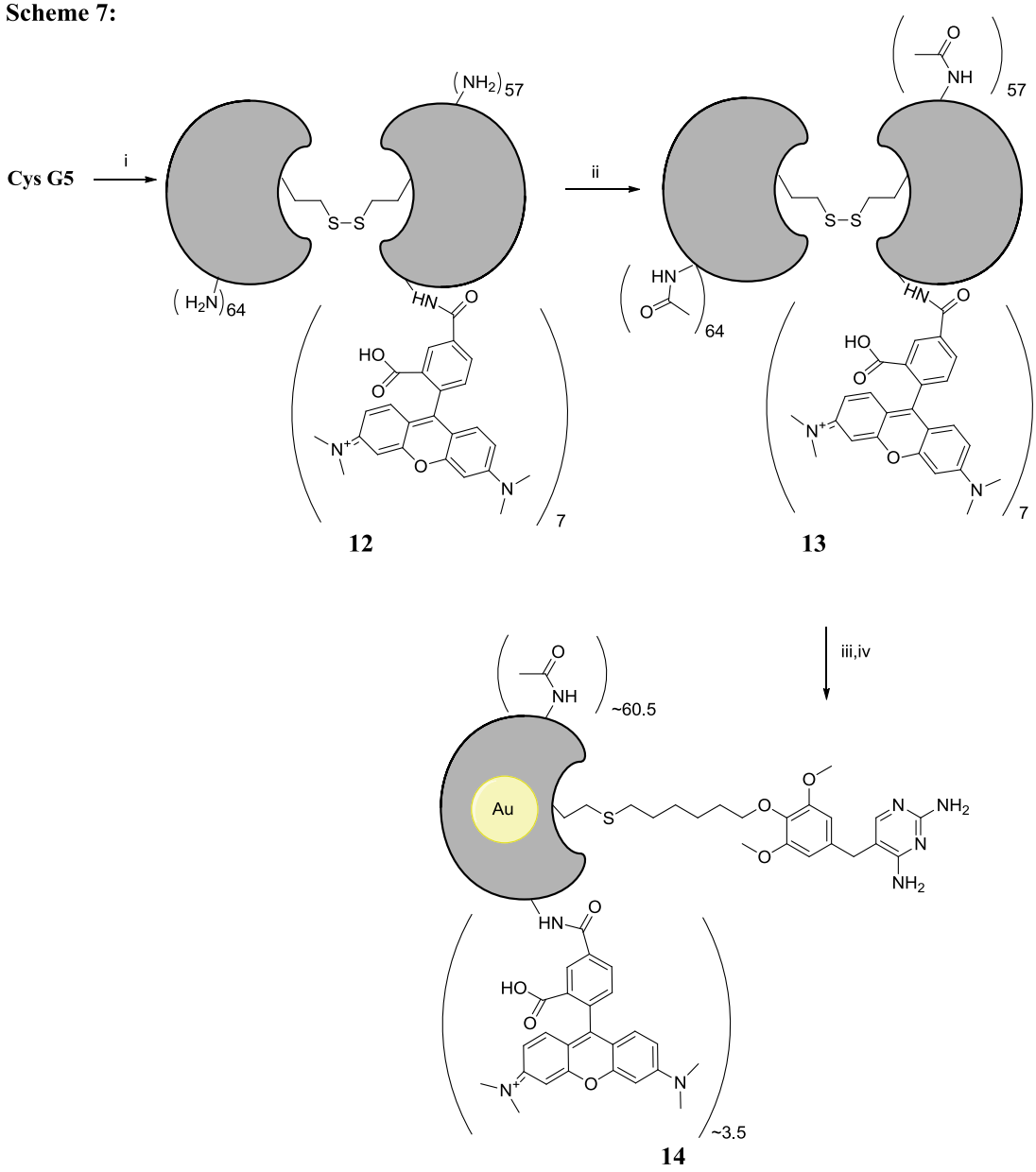


Reaction: i) TAMRA, HBTU, HOBT, TEA, DMF ii) Acetic anhydride, TEA, MeOH iii) TCEP.HCl, $H_2O$; TMP-I, NaOMe, DMF iv) $HAuCL_4$, $NaBH_4$ in 0.3M NaOH

### 3.2.2.14 Gold particle templating.

The same procedure was followed for **1,2,3,6,7,8**,**11** and **14** (95). 5 nmol dendrimer was dissolved in 500 µL $H_2O$. To this, 55 eq of 2 mM $HAuCl_4$ was added and vigorously stirred for

20 mins. 275 eq of $NaBH_4$ in 0.3M NaOH was added quickly while stirring. The color changed from yellow to brown. **8** was also labeled with 140 eq Au following the same procedure.

### 3.2.2.15 Characterization

**NMR:** Dendrimer surface passivation was achieved by two different approaches: hydroxylation and acetylation. NMR was used to determine the extent of passivation. To determining the extent of hydroxylation for **1** and **10,** the area of the methine proton of the glycidol moiety (3.78 ppm) adjoining the hydroxyl group was compared to the area of the methylene protons (2.37 ppm) within the dendrimer backbone (Scheme 1) (98). The extent of acetylation for **2, 3** and **13** was also calculated using a known procedure. The integration of the peak at 1.84 ppm from the methyl protons of the acetyl group was compared to the integration of the peak at 2.37 ppm from the dendrimer backbone.

**UV-VIS**: The absorbance spectra of 9 and 13 were used to estimate the number of TAMRA per dendrimer (Figure 16). The concentration of TAMRA was calculated using the measured absorbance at 560 nm and the extinction coefficient (91,000 $M^{-1}$ $cm^{-1}$). This was divided by the concentration of the dendrimer to get the average number of TAMRA per dendrimer.

Gold nanoparticles larger than 2 nm in size typically have a surface plasmon band between 500 to 550 nm. To verify the size of the nanoparticles, absorbance spectra was taken from 800 nm to 300 nm.

**HABA Avidin:** When HABA (2-hydroxyazobenzen-4'-carboxylic Acid) is bound to avidin, it forms a yellow-orange colored complex that absorbs at 500 nm. When biotin is added because of its high affinity for avidin, it displaces HABA easily causing the absorbance to

decrease. HABA avidin test was done for **8** and **11** to determine the amount of biotin present and hence the purity of the compound. HABA/Avidin reagent obtained from Sigma Aldrich was reconstituted in 10 mL deionized water. 900 µl of this was added to a 1 ml cuvette and the absorbance measured at 500 nm. To this 100 µl of the sample was added and the absorbance measured again. Change in absorbance, $\Delta A_{500} = 0.9( A_{HABA/avidin}) - A_{HABA/avidin+sample}$. Biotin concentration in µmol/ml = $(\Delta A_{500}/34)(10)$ where 34 is the $mM^{-1}$ extinction coefficient at 500 nm and 10 is the dilution factor of sample into the cuvette. As moles of biotin = moles of product we calculated the mass of the product and then subtracted it from the total mass used for the assay. The difference mass was assumed to be the unreacted dendrimer. The mass of the product and unreacted dendrimer were used to calculate the moles of each and, hence, the purity of the sample.

**Ellman's test:** Reaction with Ellman's reagent was used as another measure of purity for ligand-functionalized dendrimers **6**. Thiols react with Ellman's reagent (5,5'-dithiobis-(2-nitrobenzoic acid) or DTNB by cleaving the disulfide bond giving 2-nitro-5-thiobenzoate ($NTB^-$) which is yellow in color and has an absorbance at 412 nm. 50 µl of the sample solution (~0.6 mM) was added to 1ml of 0.1 M phosphate buffer, pH 8, and 10 µl of 200 mM DTT and stirred for 2 hours. DTT was removed by centrifugation using a filter device with a MWCO of 3000. The solution was added to a cuvette with 1000 µl phosphate buffer and 50 µl Ellman's reagent (4mg/ml). The absorbance was measured at 412 and subtracted from the absorbance of a blank comprised of Ellman's solution and phosphate buffer. The concentration was determined by using the change in absorbance and the extinction coefficient of the $NTB^-$ (14150 $M^{-1}cm^{-1}$)

**LRET binding affinity assays:** The binding affinity of **6** and **7** for eDHFR was determined by measuring the decrease in $Tb^{3+}$-to-GFP LRET in time-resolved mode when **6** or **7** were added to solutions of TMP-TTHA-cs124(-Tb) and eDHFR-GFP. eDHFR-GFP (20 nM) and TMP-TTHA-cs124 Tb(20 nM) were titrated in 96-well plates with **6** or **7** at concentrations ranging from ~10 nM to 20 μM in assay buffer (50 mM $K_2HPO_4$, $KH_2PO_4$, 18 mMβ-mercaptoethanol, 20 μM NADPH, pH 7.2). Time-resolved luminescence (time delay = 100 μs; measurement window = 1400 μs, $\lambda_{ex}$ = 340/60 nm) was measured at $\lambda_{em}$ = 520/10 nm (LRET-sensitized GFP emission signal) and at $\lambda_{em}$ = 615/10 nm ($Tb^{3+}$ donor signal). For each well, the ratios of the emission signals at the indicated wavelengths (520/615) for the sample well was calculated and plotted against the concentration of **6** or **7**. As a control, a similar assay was done using **2** and **3**.

**SDS PAGE electrophoresis:** SDS-PAGE was performed on 15% polyacrylamide gel at room temperature for 1 hour at 170 V. Coomassie R250 was used for staining.

**TEM**: The dendrimer encapsulated nanoparticles were characterized using TEM. TEM was performed using a JEOL JEM-3010. The microscope is equipped with a LaB6 electron source. Accelerating voltage was 300kV. Images were acquired with a Gatan 1K x 1K slow-scan CCD camera. For preparing the samples, 5 μL of the solution was placed on carbon coated copper grids and the solvent was allowed to air dry. From the TEM images, a histogram for the size distribution of the nanoparticles was plotted.

## 3.3 Results

### 3.3.1 Functionalization with TAMRA

Labeling of TAMRA of G4 and G5 dendrimers was done using HOBT, HBTU and TEA as the coupling reagents. NMR of the TAMRA labeled dendrimers **9**, **10**, **11**, **13** and **14** showed the aromatic peaks of TAMRA. The number of TAMRA molecules of TAMRA per dendrimer for G4-TAMRA (**9)** and G5-TAMRA-Ac (**13**) were determined to be 2 and 7 by UV.

### 3.3.2 Surface passivation

To prepare dendrimers with electrostatically neutral surfaces, passivation of surface amines with glycidol or acetamide was performed using established procedures (98). For glycidol passivation of G4 dendrimers (69)**,** NMR integration analysis showed 95 glycidol per particle. Since there are approximately 64 primary amines on the surface, it means that some amines were labeled with two glycidol groups. Glycidol passivation of G4-TAMRA-OH (**10**) showed 69 glycidol groups by NMR. For acetamide passivation (G4-Ac, **2**; G5-Ac, **3,** G5-TAMRA-Ac, **13**), complete acetylation of the surfaces was determined by NMR.

Table 4. Summary of purification methods, purities, and results of TEM size characterization for all Dendrimer Encapsulated Nanoparticles.

| Compound | Purification method | Percentage purity (analysis) | DEN size |
|---|---|---|---|
| G4-OH (69) | Centrifugal filtration | 95 glycidols/dendrimer (NMR, MALDI) | ~ 2nm |
| G4-OH-Biotin (**8**) +55 Au | Not purified | 78% (HABA) | ~ 2.2 nm |
| G4-OH-Biotin (**8**) +140 Au | Not purified | 78% (HABA) | ~ 3 nm |
| G4-TAMRA-OH-Biotin (**11**) | Not purified | 64% (HABA) | Not determined [1] |
| G4-Ac (**2**) | Centrifugal Filtration | 100% acetylation (NMR, MALDI) | ~1.8 nm |
| G4-Ac-TMP (**6**) | HPLC | >95 % (SDS-PAGE. Ellman Test) | Not determined.[2] |
| G5-Ac (**3**) | Centrifugal Filtration | NMR, MALDI show complete acetylation | ~ 2.0 nm |
| G5-Ac-TMP (**7**) | Size exclusion chromatography | >95 % (SDS-PAGE)[3] | ~2.0 nm |
| G5-TAMRA-Ac-TMP (**14**) | Not purified | ~50 % (SDS-PAGE) | ~1.8 nm |

[1]TAMRA fluorescence was substantially quenched with gold analog of **11**, suggesting size > 2 nm. [2]Gold templating resulted in sample precipitation. [3]Ellman's Test was unsuccessful for **7.**

Table 4

### 3.3.3 Reduction of cystamine cores and functionalization with thiol-reactive ligands moieties

Following disulfide reduction and reaction with biotin-maleimide, NMR analysis of G4-OH-biotin (**8**) showed the multiplet peaks at 1.5, 1.6, and 1.7 from the $CH_2$ protons in biotin but they were too small for integration. The product **8** was determined to be 78% pure using HABA assay. SDS PAGE showed a band below the G4-OH band (Figure 13). The product G4-TAMRA-OH-Biotin **11** was determined to be 64 % pure using HABA assay. The NMR spectra of unpurified G4-Ac-TMP (**6**) and G5-Ac-TMP (**7**) showed two aromatic peaks at 6.5 and 7.5 ppm, corresponding to the aromatic peaks of TMP. However, the amounts of the purified products were too small for NMR characterization. Purification by HPLC (**6**) or size-exclusion chromatography (**7**) yielded products that were >95% pure, as judged by SDS-PAGE analysis. The product G5-TAMRA-Ac-TMP (14) was determined to be ~50% pure by SDS PAGE (Figure 13).

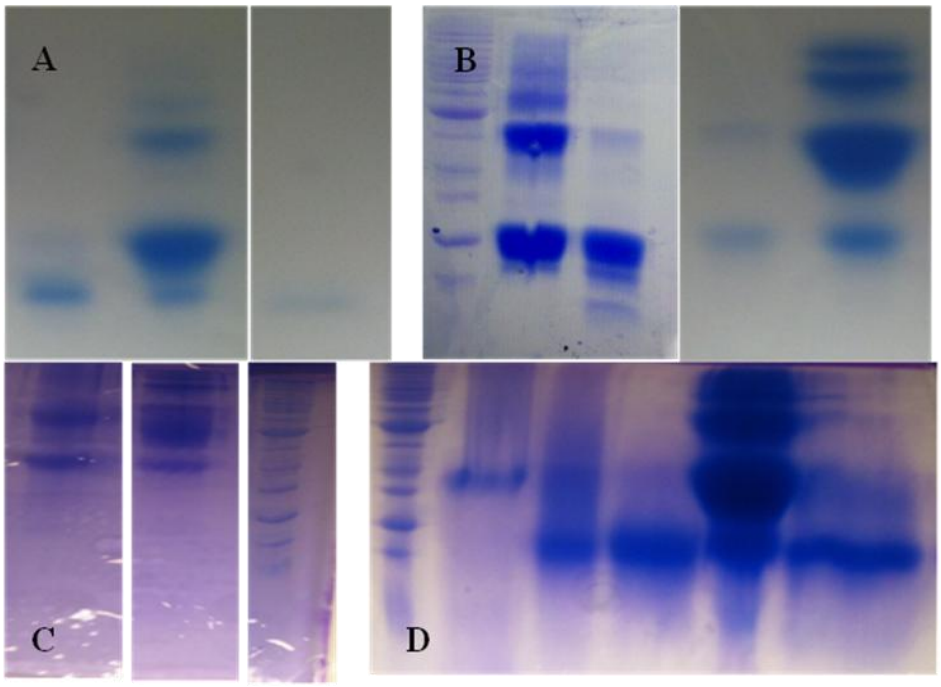


Figure 13: SDS-PAGE images. 13A: From left to right: G4-Ac-TMP (6) impure, G4-Ac (2), G4-Ac-TMP (6) pure. 13B: From left to right: protein ladder, crude G5-Ac-TMP (7), pure G5-Ac-TMP (7), crude G5-Ac-TMP (7), G5-Ac (3). 13C: left to right: G5-TAMRA-Ac-TMP (14), G5-TAMRA-Ac (13), protein ladder. 13D: from left to right: protein ladder, Cys G4, G4-TAMRA-OH, G4-TAMRA-OH-Biotin, G4-OH, G4-OH-Biotin.

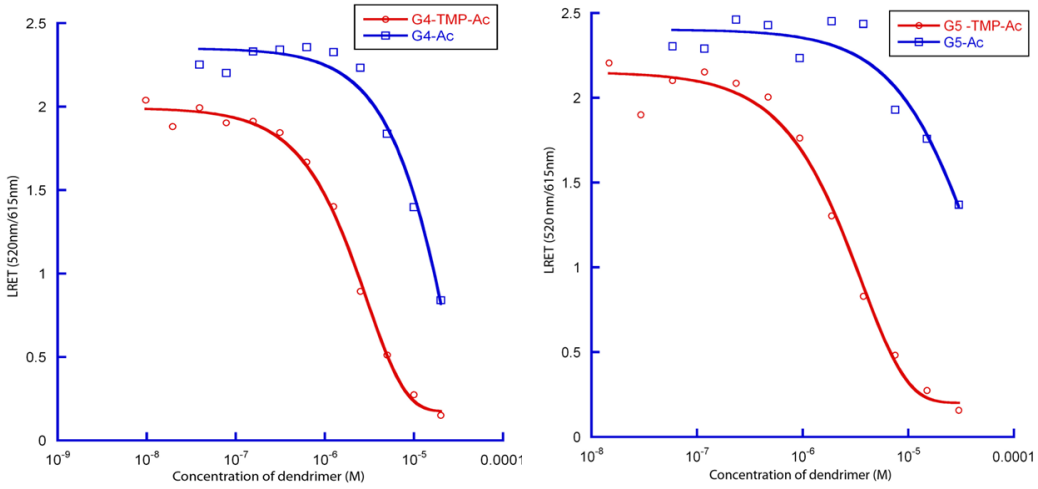


Figure 14: LRET binding assays. The figure on the left shows decrease in LRET between TMP-TTHA-cs124 Tb and eDHFR-GFP with increase in concentration of G4-TMP-Ac and the second one is a similar assay with G5-TMP-Ac.

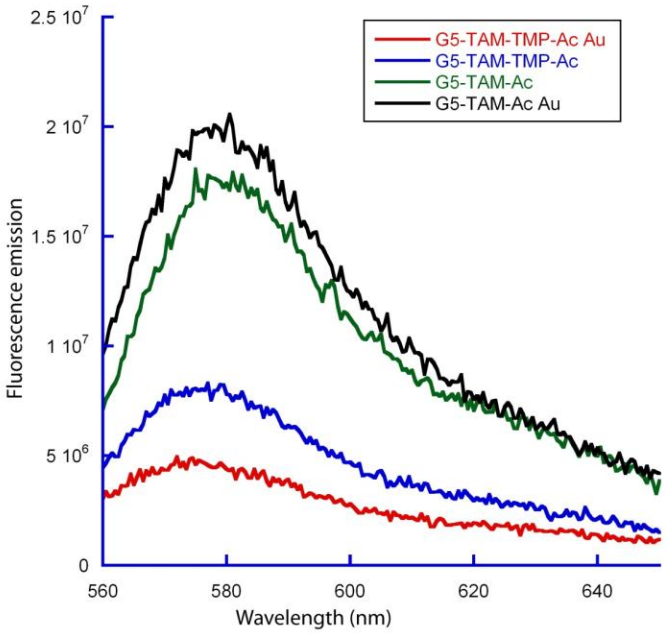


Figure 15: Fluorescence emission spectra of G5-TAMRA-TMP-Ac $(Au)_{55}$, G5-TAMRA-TMP-Ac, G5-TAMRA-Ac and G5-TAMRA-Ac $(Au)_{55}$

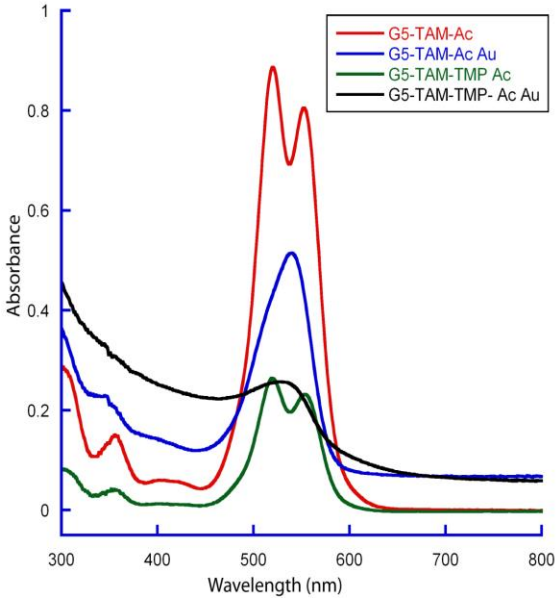


Figure 16: UV-Vis spectra of aqueous solutions of G5-TAMRA-Ac, G5-TAMRA-Ac $(Au)_{55}$, G5-TAMRA-TMP-Ac and G5-TAMRA-TMP-Ac $(Au)_{55}$

### 3.3.4 LRET Binding Assays.

Binding affinity of **6** and **7** towards eDHFR was determined by LRET binding assays. Although **6** and **7** showed decrease in LRET between TMP-TTHA-cs124 Tb and eDHFR-GFP with increase in concentration indicating that **6** and **7** displace TMP-TTHA-cs124 $Tb^{3+}$ from eDHFR, the controls (**2** and **3**) also showed some decrease (Figure 14) which could be because of non specific interaction between the dendrimer and the protein. Binding assays could not be done with gold labeled **7** because gold quenched GFP fluorescence.

### 3.3.5 Au nanoparticle templating.

The gold nanoparticles formed with 55 equivalent Au and hydroxylated dendrimers were between 2 and 2.2 nm (**1** and **8**). With 140 eq, Au gold nanoparticle formed from **8** had an average size of 3 nm. DENs formed from acetylated dendrimers (**2**, **3**,**7** and **14**) were slightly smaller and ranged from 1.8 -2 nm in size. Gold encapsulation of **6** could not be achieved. The gold crashed out of the solution and agglomerates could be seen in the TEM images. Fluorescence emission of TAMRA in the case of **13** and **14** decreased but was not completely quenched after gold nanoparticle formation (Figure 15). The absorption spectra of **13** and **14** also showed some change after gold nanoparticle formation. Prior to gold labeling two peaks were seen for both **13** and **14** which is in line with earlier work wherein the TAMRA peak spilt into two after protein conjugation (99). After gold encapsulation however, there was just one absorbance peak for each (Figure 16). UV-vis absorption spectra of almost all the nanoparticles showed a slight surface Plasmon band at ~ 550 nm. In the case of G4-OH-Biotin $Au_{140}$, the peak was more prominent. This agrees more or less with earlier work according to which gold nanoparticles more than 2 nm in size show a surface Plasmon band (95).

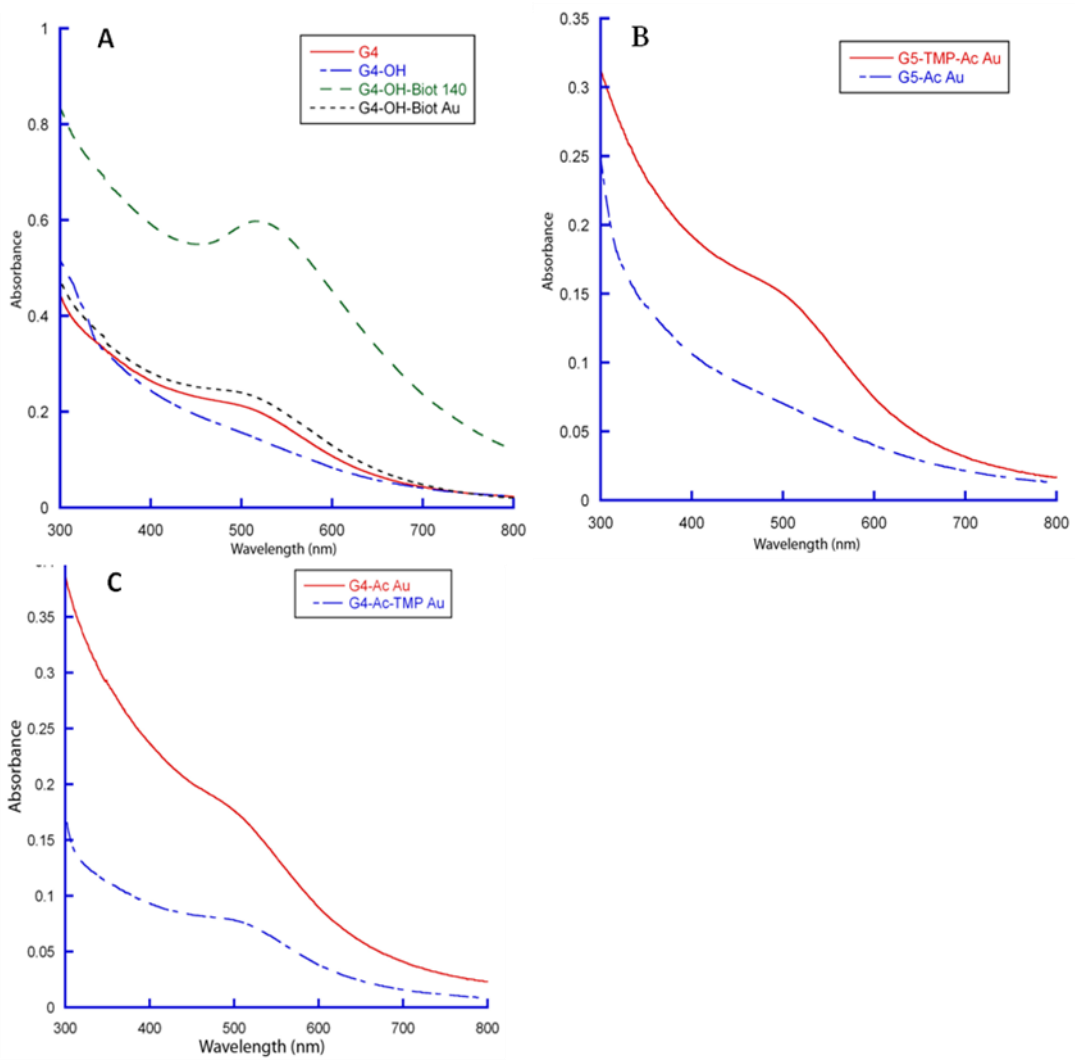


Figure 17: Absorption spectra of DENs. 17A: Absorption spectra of DENs of G4, G4-OH (69), G4-OH-Biotin (8) (140 Au), G4-OH-Biotin (**8**) (55 Au). 17B: Absorption spectra of DENs of G5-TMP-Ac (**7**) an G5-Ac (**3**). 17C: Absorption spectra of DENs of G4-TMP-Ac (**6**), G4-Ac (2).

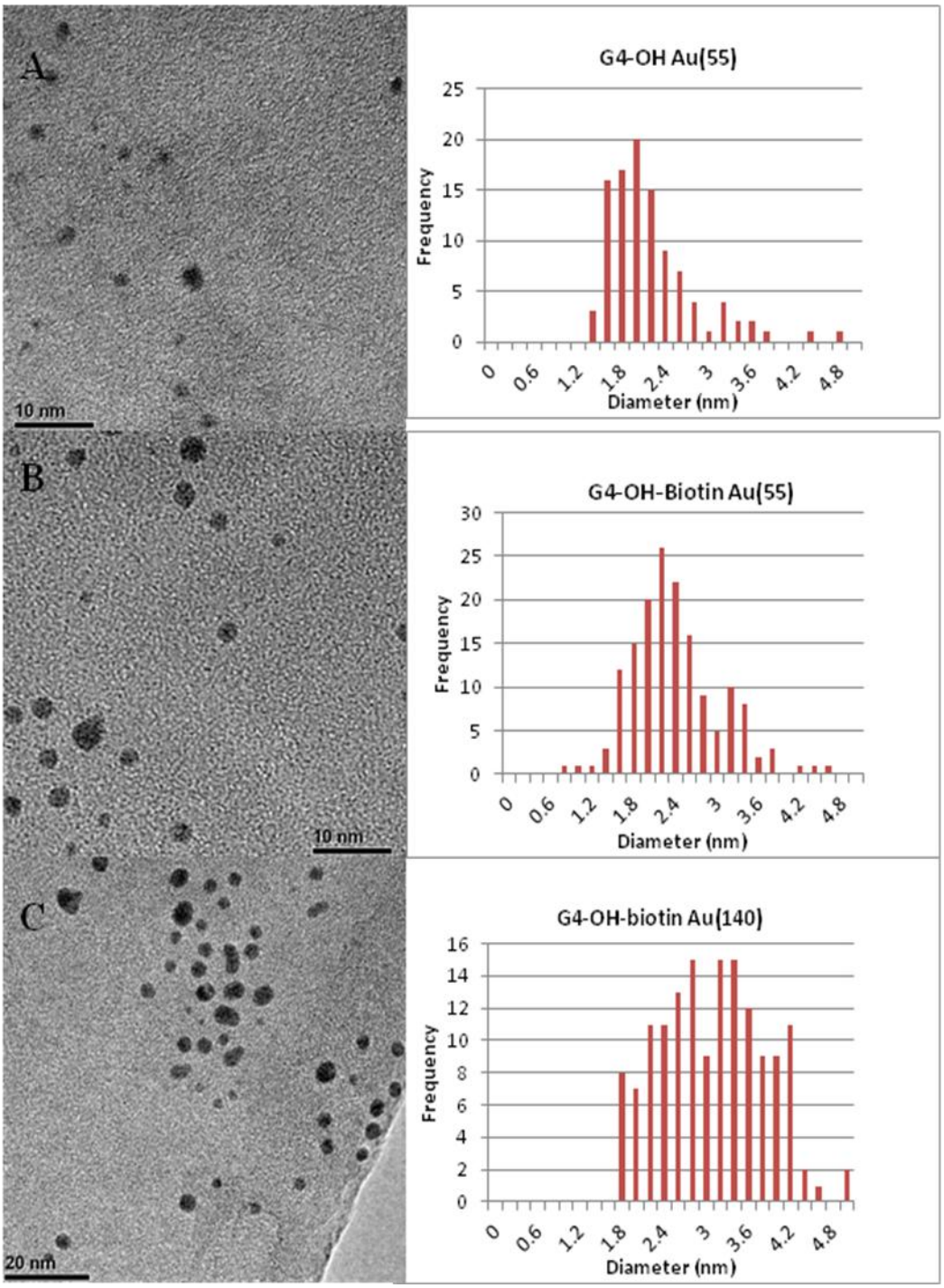


Figure 18: TEM images and the corresponding histograms for G4-OH (**A**), G4-OH-Biotin $(Au)_{55}$ (**B**) and G4-OH-Biotin $(Au)_{140}$ (**B**).

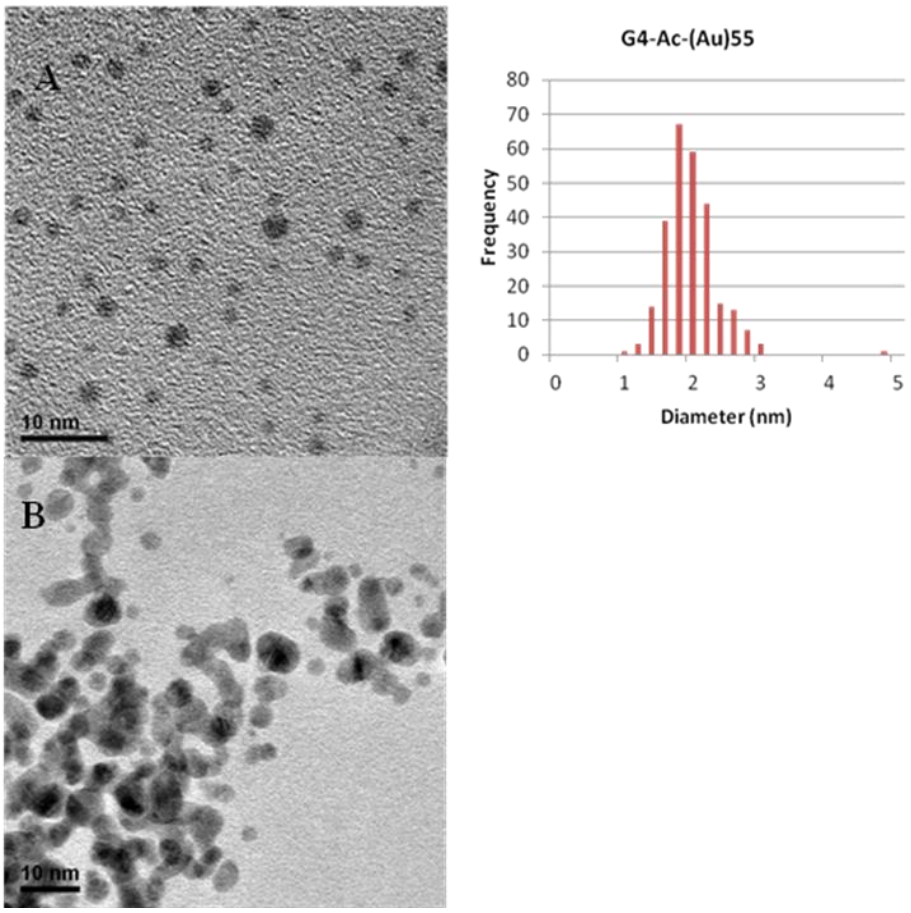


Figure 19: TEM images and the corresponding histograms for G4-Ac $(Au)_{55}$ (A), G4-TMP-Ac $(Au)_{55}$ (B). G4-TMP-Ac $(Au)_{55}$ precipitated out.

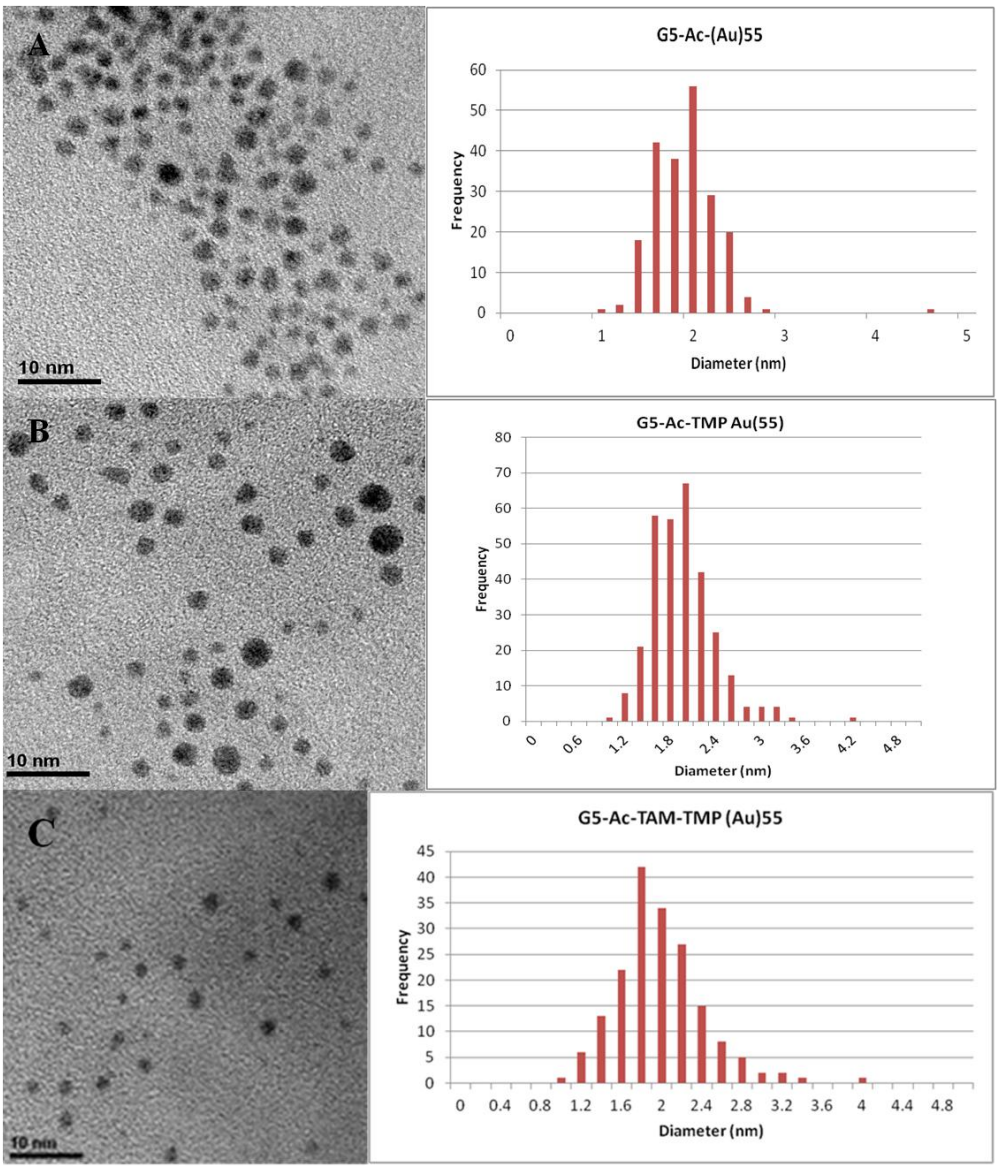


Figure 20: TEM images and the corresponding histograms for G5-Ac $(Au)_{55}$ (**A**), G5-TMP-Ac $(Au)_{55}$ (**B**) and G5-Ac-TAM-TMP $(Au)_{55}$ (**C**).

### 3.4 Discussion

The initial objective of this study was to prepare dendrimer-based probes that: i) possessed a single, protein-targeting ligand (e.g., trimethoprim); ii) contained multiple fluorophores that would allow efficient detection by light microscopy; and iii) encapsulated a gold nanoparticle that would generate contrast when imaged with an electron microscope. With such structures, we envisioned a strategy where cultured cells would be made to express proteins fused to eDHFR. Upon fixation and staining with the dendrimer probes, the eDHFR fusion proteins would be selectively labeled and made visible for CLEM studies. We desired dendrimers labels that contained a single ligand to allow for precise labeling of target proteins.

In general, attaching a single small molecule to a nanoparticle is challenging because of their large size and multiple reactive surface moieties. Nevertheless, monovalent functionalization is desirable for biological applications where multiple ligands might cause unwanted oligimerazation of proteins or other targets. Gold nanocrystal conjugates bearing a discrete number of single-stranded DNA oligomers have been purified using gel electrophoresis (100). Other gold clusters linked to a fluorophore and antibody Fab' fragments have been purified by gel filtration, yielding ca. 80% monovalency (36) (96). More recently, electrophoresis of CdSe nanocrystal-DNA conjugates has been used to obtain monovalent structures for biolabeling and fluorescence microscopy (97) (101). Besides their potential application as multimodal imaging contrast agents, we were also intrigued by the general possibility of using cystamine-core, PAMAM dendrimers as scaffolds for preparing a variety of monovalently functionalized nanoparticles.

Our synthetic strategy was based on well established dendrimer manipulations, and the overall reaction order was as follows: i) optional conjugation of multiple fluorophores (e.g., TAMRA) to surface amines; ii) passivation of remaining primary amines with glycidol or acetic anhydride; iii) reduction of core disulfide followed by reaction with maleimide- or iodide-functionalized ligands; iv) templated formation of gold nanoparticles with functionalized dendrons. Conjugation of multiple fluorophores to the terminal amines of PAMAM dendrimers is synthetically straightforward. We successfully prepared G4 and G5 dendrimers that contained, on average, two and seven TAMRA molecules, respectively. Furthermore, subsequent passivation of the remaining terminal amines with glycidol or acetic anhydride did not seem to affect TAMRA fluorescence. The surface passivation step is critical for preventing non-specific reaction of electrophilic, thiol-reactive ligands with nucleophilic surface amines and for generating electrostatically neutral structures. While purification following fluorophore conjugation and surface capping is straightforward using membrane dialysis, it proved difficult to separate ligand-conjugated dendrons from unreacted starting materials. As can be seen from the results of HABA assays on biotin-conjugated, G4-OH dendrons (**8**, **11),** the reduction and subsequent reaction with thiol-reactive, biotin-maleimide yielded products that were only 60%-70% pure. We successfully used HPLC to purify G4-Ac-TMP (**6**), and G5-Ac-TMP could be purified using size-exclusion chromatography. Attempts to purify other ligand-dendron conjugates were unsuccessful.

Templating with 55 equivalents of gold yielded nanoparticles with a similar size distribution and mean diameters of 1.8-2.2 nm, while particles formed with 140 gold equivalents were approximately 3 nm in diameter (Table 4). The size distribution of 55-atom particles was independent of dendrimer template generation (G4 or G5) and surface chemistry (hydroxyl or

acetamide capping). Moreover, a similar size distribution was observed when a purified, ligand-functionalized dendron (G5-Ac-TMP, **7**) was used as a template. These results would seem to suggest that dendrons with molecular weights approximately half of the parent dendrimers are effective templates for gold nanoparticle encapsulation. However, the particle sizes that we observe are larger than those predicted by theory and previously reported in the literature. Earlier studies reported that DENs formed from G4-G6 dendrimers and 55 gold equivalents had diameters of ~1.3 nm. With 140 equivalents, the size increased to 1.6 nm (95). Crooks and co-workers reported that surface hydroxyls can prematurely reduce gold ions, resulting in the formation of large clusters (95). However, we see similar results with hydroxylated and acetylated templates. At this point, we cannot rule out the possibility that our templating process is actually yielding gold particles that are stabilized by multiple dendritic structures, as opposed to being encapsulated within a single entity. Such surface-stabilization has been reported when amine-terminated, G4 dendrimers were reacted with 55 gold equivalents (102).

Although Crooks et al. have reported synthesis of 1.3 nm G4-NH2 encapsulated gold nanoparticles, when Hoffman et al. repeated the synthesis using the same methodology, they reported nanoparticles which were 2.7 nm in size on average. This suggests that gold nanoparticle encapsulation within dendrimers is not a well-understood process. Future work could be the determination of the exact structure of the dendrimer stabilized gold nanoparticles using methods like atomic force microscopy phase imaging, X-ray scattering studies, and staining the dendrimer with phosphotungstic acid solution for TEM.

# Chapter 4

# REFERENCES

1. Tsien R. 2003. *Nature reviews. Molecular cell biology* Suppl
2. Lakowicz J. 2006. *Principles of Fluorescence Spectroscopy* New York: Springer
3. Degorce F. 2009. *Curr Chem Genomics* 3: 22-32
4. Connally RE, Piper JA. 2008. *Annals of the New York Academy of Sciences* 1130: 106-16
5. Bunzli J. 2010. *Chem Rev* 110: 2729–55
6. RC Leif LV, MC Becker, S Yang 2006. *Cytometry A* 69A: 767–78
7. Selvin PR. 2002. *Annual Review of Biophysics and Biomolecular Structure* 31: 275-302
8. Botchway SW, Charnley M, Haycock JW, Parker AW, Rochester DL, et al. 2008. *Proceedings of the National Academy of Sciences* 105: 16071-6
9. RR de Haas RvG, EB van der Tol, J Veuskens, HE van Gijssel, RB Tijdens, J Bonnet, NP Verwoerd, HJ Tanke. 1999

*J Histochem Cytochem* 47: 183–96

10. RR de Haas RvG, EB van der Tol, HJ Zijlmans, T Bakker-Schut, J Bonnet,NP Verwoerd, HJ Tanke. 1997. *J Histochem Cytochem* 45: 1279–92
11. S Phimphivong SK, PL Edmiston, SS Saavedra. 1995. *Analytica Chimica Acta* 307: 403-17
12. Hennink EJ, de Haas R, Verwoerd NP, Tanke HJ. 1996. *Cytometry* 24: 312-20
13. D Jin RC, J Piper. 2006 *Journal of Physics D: Applied Physics* 39: 461-5
14. Connally R, Jin D, Piper J. 2006. *Cytometry Part A* 69A: 1020-7
15. AE Soini AK, NJ Meltola. 2003. *Microscopy Research and Technique* 62: 396-407
16. Verwoerd NP, Hennink EJ, Bonnet J, Van der Geest CRG, Tanke HJ. 1994. *Cytometry* 16: 113-7
17. Kenneth R. 1998. *Methods in Cell Biology* 81: 171-84
18. I Rasnik TF, K Jacobson, K Berland. 2007. *Methods in Cell Biology* 81: 219-49
19. VK Ramshesh JL. 2008. *journal of Biomedical Optics* 13: 064001
20. Born M, Wolf E. 1997. *Principles of optics: electromagnetic theory of propagation, interference and diffraction of light*: Cambridge University Press
21. Hell SW. 2009. *Nat Meth* 6: 24-32
22. Vicidomini G, Gagliani MC, Cortese K, Krieger J, Buescher P, et al. 2010. *Microscopy Research and Technique* 73: 215-24
23. Garini Y, Vermolen BJ, Young IT. 2005. *Current Opinion in Biotechnology* 16: 3-12
24. Egerton RF. 2005. *Physical principles of electron microscopy : an introduction to TEM, SEM, and AEM /*
25. Sosinsky GE, Giepmans BNG, Deerinck TJ, Gaietta GM, Ellisman MH. 2007. In *Methods in Cell Biology*, ed. JR McIntosh, pp. 575-91: Academic Press
26. Cortese K, Diaspro A, Tacchetti C. 2009. *Journal of Histochemistry & Cytochemistry* 57: 1103-12
27. Mironov AA, Beznoussenko GV. 2009. *Journal of Microscopy* 235: 308-21
28. Webster P, Schwarz H, Griffiths G. 2008. In *Methods in Cell Biology*, ed. DA Terence, pp. 45-58: Academic Press
29. Weston A, Armer H, Collinson L. 2010. *Journal of chemical biology* 3: 101-12
30. Agronskaia AV, Valentijn JA, van Driel LF, Schneijdenberg CTWM, Humbel BM, et al. 2008. *Journal of Structural Biology* 164: 183-9
31. Capani F, Ellisman MH, Martone ME. 2001. *Brain Research* 923: 1-11
32. Shu X, Lev-Ram V, Deerinck T, Qi Y, Ramko E, et al. 2011. *PLoS Biol* 9: e1001041

33. Nisman R, Dellaire G, Ren Y, Li R, Bazett-Jones DP. 2004. *Journal of Histochemistry & Cytochemistry* 52: 13-8
34. Powell RD, Halsey CMR, Hainfeld JF. 1998. *Microscopy Research and Technique* 42: 2-12
35. Takizawa T, Robinson JM. 2000. *Journal of Histochemistry & Cytochemistry* 48: 433-6
36. Powell RD, Halsey CMR, Spector DL, Kaurin SL, McCann J, Hainfeld JF. 1997. *Journal of Histochemistry & Cytochemistry* 45: 947-56
37. Robinson JM, Vandré DD. 1997. *Journal of Histochemistry & Cytochemistry* 45: 631-42
38. Giberson RT, Demaree RS. 1994. *Microscopy Research and Technique* 27: 355-7
39. Esfand R, Tomalia DA. 2001. *Drug Discovery Today* 6: 427-36
40. Menjoge AR, Kannan RM, Tomalia DA. 2010. *Drug Discovery Today* 15: 171-85
41. Tomalia DA. 1996. *Macromolecular Symposia* 101: 243-55
42. D.A.Tomalia HB, J. Dewald, M. hall, G. Kallos, S. Martin, J. Roeck, J. Rider, P. Smith. 1985. *Polymer Journal* 17: 117-32
43. Hawker CJ, Frechet JMJ. 1990. *Journal of the American Chemical Society* 112: 7638-47
44. Dunphy I, Vinogradov SA, Wilson DF. 2002. *Analytical Biochemistry* 310: 191-8
45. Grinstaff MW. 2002. *Chemistry – A European Journal* 8: 2838-46
46. Lee CC, MacKay JA, Frechet JMJ, Szoka FC. 2005. *Nat Biotech* 23: 1517-26
47. Tomalia D, Reyna L, Svenson S. 2007. *Biochemical Society transactions* 35: 61-7
48. Tomalia DA. 2006. *Nanomedicine : nanotechnology, biology, and medicine* 2: 309
49. Wiener E, Brechbiel MW, Brothers H, Magin RL, Gansow OA, et al. 1994. *Magnetic Resonance in Medicine* 31: 1-8
50. Stiriba S-E, Frey H, Haag R. 2002. *Angewandte Chemie International Edition* 41: 1329-34
51. Longmire M, Choyke PL, Kobayashi H. 2008. *Current Topics in Medicinal Chemistry* 8: 1180-6
52. Vohs JK, Fahlman BD. 2007. *New Journal of Chemistry* 31: 1041-51
53. Zhao M, Sun L, Crooks RM. 1998. *Journal of the American Chemical Society* 120: 4877-8
54. Myers VS, Weir MG, Carino EV, Yancey DF, Pande S, Crooks RM. 2011. *Chemical Science* 2: 1632-46
55. Scott RWJ, Wilson OM, Crooks RM. 2004. *The Journal of Physical Chemistry B* 109: 692-704
56. Esumi K, Suzuki A, Aihara N, Usui K, Torigoe K. 1998. *Langmuir* 14: 3157-9
57. Zheng J, Dickson RM. 2002. *Journal of the American Chemical Society* 124: 13982-3
58. Zhao M, Crooks RM. 1999. *Chemistry of Materials* 11: 3379-85
59. Lemon BI, Crooks RM. 2000. *Journal of the American Chemical Society* 122: 12886-7
60. Gröhn F, Bauer BJ, Akpalu YA, Jackson CL, Amis EJ. 2000. *Macromolecules* 33: 6042-50
61. Murray J, Appleton P, Swedlow J, Waters J. 2007. *Journal of Microscopy* 228: 390-405
62. Lesniak W, Bielinska AU, Sun K, Janczak KW, Shi X, et al. 2005. *Nano Letters* 5: 2123-30
63. Xiangyang Shi TRG, Kai Sun, Lajos P Balogh, James R Baker Jr. 2006. *Nanotechnology* 17: 1072-8
64. Balogh L, Swanson DR, Tomalia DA, Hagnauer GL, McManus AT. 2000. *Nano Letters* 1: 18-21

65. Bauer H, Blanc J, Ross DL. 1964. *Journal of the American Chemical Society* 86: 5125-31
66. Wittmershaus BP, Skibicki JJ, McLafferty JB, Zhang Y-Z, Swan S. 2001. *Journal of Fluorescence* 11: 119-28
67. Crosby GA, Demas JN. 1971. *The Journal of Physical Chemistry* 75: 991-1024
68. Grunwald D, Shenoy SM, Burke S, Singer RH. 2008. *Nat. Protocols* 3: 1809-14
69. Conchello JWLJ-A. 2005. *Nature Methods* 12: 10
70. Leif RC YS, Jin D, Piper J, Vallarino LM, Williams JW, Zucker RM. 2009. *Journal of Biomedical Optics* 14
71. Marriott G, Clegg RM, Arndt-Jovin DJ, Jovin TM. 1991. *Biophysical Journal* 60: 1374-87
72. Härmä H, Soukka T, Lövgren T. 2001. *Clinical Chemistry* 47: 561-8
73. Petoud S, Cohen SM, Bünzli J-CG, Raymond KN. 2003. *Journal of the American Chemical Society* 125: 13324-5
74. Okada CY, Rechsteiner M. 1982. *Cell* 29: 33-41
75. Rechsteiner M. 1987. *methods enzymology* 149: 42–8
76. Rajapakse H, Gahlaut N, Mohandessi S, Yu D, Turner J, Miller L. 2010. *Proceedings of the National Academy of Sciences of the United States of America* 107: 13582-7
77. Montgomery CP, Murray BS, New EJ, Pal R, Parker D. 2009. *Accounts of Chemical Research* 42: 925-37
78. Song B, Vandevyver CDB, Chauvin A-S, Bunzli J-CG. 2008. *Organic & Biomolecular Chemistry* 6: 4125-33
79. Rajapakse HE, Reddy DR, Mohandessi S, Butlin NG, Miller LW. 2009. *Angewandte Chemie International Edition* 48: 4990-2
80. Thibon A, Pierre V. 2009. *Analytical and Bioanalytical Chemistry* 394: 107-20
81. Tsien RY. 1998. *annual review of biochemistry* 67: 509-44
82. Sala F, Hernández-Cruz A. 1990. *Biophysical Journal* 57: 313-24
83. Condrau MA, Schwendener RA, Niederer P, Anliker M. 1994. *Cytometry* 16: 187-94
84. Condrau MA SR, Zimmermann M, Muser MH, Graf U, Niederer P, Anliker M. 1994. *Cytometry* 16: 195-205.

85. Jin D, Connally R, Piper J. 2007. *Cytometry Part A* 71A: 783-96
86. Jin D, Connally R, Piper J. 2007. *Cytometry Part A* 71A: 797-808
87. Moore EG, Samuel APS, Raymond KN. 2009. *Accounts of Chemical Research* 42: 542-52
88. Leif RC, Vallarino LM, Becker MC, Yang S. 2006. *Cytometry Part A* 69A: 940-6
89. Jiang L, Wu J, Wang G, Ye Z, Zhang W, et al. 2010. *Analytical Chemistry* 82: 2529-35
90. Wu J, Wang G, Jin D, Yuan J, Guan Y, Piper J. 2008. *Chemical Communications*: 365-7
91. Wu J, Ye Z, Wang G, Jin D, Yuan J, et al. 2009. *Journal of Materials Chemistry* 19: 1258-64
92. Miller LW, Sable J, Goelet P, Sheetz MP, Cornish VW. 2004. *Angewandte Chemie International Edition* 43: 1672-5
93. Miller LW, Cai Y, Sheetz MP, Cornish VW. 2005. *Nat Meth* 2: 255-7
94. Calloway NT, Choob M, Sanz A, Sheetz MP, Miller LW, Cornish VW. 2007. *ChemBioChem* 8: 767-74
95. Kim Y-G, Oh S-K, Crooks RM. 2003. *Chemistry of Materials* 16: 167-72
96. Hainfeld JF, Furuya FR. 1992. *J. Histochem. Cytochem.* 40: 177-84

97. Howarth M, Liu W, Puthenveetil S, Zheng Y, Marshall LF, et al. 2008. *Nat Meth* 5: 397-9
98. Oh S-K, Niu Y, Crooks RM. 2005. *Langmuir* 21: 10209-13
99. Ravdin P, Axelrod D. 1977. *Analytical Biochemistry* 80: 585-92
100. Zanchet D, Micheel CM, Parak WJ, Gerion D, Alivisatos AP. 2000. *Nano Letters* 1: 32-5
101. Liu HY, Gao X. 2011. *Bioconjugate Chemistry* 22: 510-7
102. Hoffman LW, Andersson GG, Sharma A, Clarke SR, Voelcker NH. 2011. *Langmuir* 27: 6759-67

# Chapter 5

# VITA

**Name:** **Nivriti Gahlaut**

**Education:**

| | | |
|---|---|---|
| St Stephens College, Delhi University | Chemistry, BSc, | 2004 |
| Indian Institute of Technology Delhi | Chemistry, MSc | 2006 |

**Protessional Experience**

| | |
|---|---|
| 2006-Present | Graduate Research Assistant, University of Illinois at Chicago, Il. |
| 2006-2008 | Teaching Assistant, University of Illinois at Chicago, Il. |
| 2005-2006 | Master's Research Assistant, IIT Delhi, Delhi, India |
| 2003 | Summer Intern, Daurala Organics Ltd, Meerut, India |

**Publications**

1. **N. Gahlaut**, L.W. Miller. Time-resolved microscopy for imaging lanthanide luminescence in living cells,*Cytometry Part A.* 2010, 77A, 12,1113-1125.
2. H. E.Rajapakse,**N. Gahlaut**,S. Mohandessi,D. Yu, J. R. Turner, L.W. Miller. Time-resolved luminescence resonance energy transfer imaging of protein–protein interactions in living cells. *Proceedings of the National Academy of Sciences*. 2010, 107,13582-13587.

**Presentations**

1. $64^{th}$ annual meeting and symposium of the society of general physiologists. Time-resolved microscopy for imaging lanthanide luminescence in living cells. Sept 7-11, 2010, Woods Hole, MA